Available online at www.sciencedirect.com
ScienceDirect
Journal of Computational Physics 224 (2007) 836–866
JOURNAL OF COMPUTATIONAL PHYSICS
www.elsevier.com/locate/jcp

High-fidelity interface tracking in compressible flows: Unlimited anchored adaptive level set

R.R. Nourgaliev *, T.G. Theofanous

Center for Risk Studies and Safety, University of California, Santa Barbara, USA

Received 31 January 2006; received in revised form 28 July 2006; accepted 22 October 2006
Available online 15 December 2006

Abstract

The interface-capturing-fidelity issue of the level set method is addressed wholly within the Eulerian framework. Our aim is for a practical and efficient way to realize the expected benefits of grid resolution and high order schemes. Based on a combination of structured adaptive mesh refinement (SAMR), rather than quad/octrees, and on high-order spatial discretization, rather than the use of Lagrangian particles, our method is tailored to compressible flows, while it provides a potentially useful alternative to the particle level set (PLS) for incompressible flows. Interesting salient features of our method include (a) avoidance of limiting (in treating the Hamiltonian of the level set equation), (b) anchoring the level set in a manner that ensures no drift and no spurious oscillations of the zero level during PDE-reinitialization, and (c) a non-linear tagging procedure for defining the neighborhood of the interface subject to mesh refinement. Numerous computational results on a set of benchmark problems (strongly deforming, stretching and tearing interfaces) demonstrate that with this approach, implemented up to 11th order accuracy, the level set method becomes essentially free of mass conservation errors and also free of parasitic interfacial oscillations, while it is still highly efficient, and convenient for 3D parallel implementation. In addition, demonstration of performance in fully-coupled simulations is presented for multimode Rayleigh–Taylor instability (low-Mach number regime) and shock-induced, bubble-collapse (highly compressible regime).

Keywords: Level set; Multi-fluid flow; Capturing interfaces; Interfacial instability; Contact discontinuities; Compressible flow; Adaptive mesh refinement; High order discretization

1. Introduction

We are working on the direct numerical simulation of interfacial instabilities in compressible multi-fluid flows and at the foundation of our approach we have adopted the level set method [28,29,35]. In a previous paper we addressed issues of coupling the flows on either side of the interface coherently with capturing the interface motion in an adaptive mesh refinement environment (as needed for the simulation of real flows of practical interest) [26]. In that development we paid special attention to the dynamics of sharp capturing at high acoustic impedance mismatch interfaces. In the present paper we focus on the kinematics of the interface

* Corresponding author. Present address: Idaho National Laboratory, Battelle Energy Alliance, LLC, P.O. Box 1625, Idaho Falls, ID 83415, United States. Tel.: +1 208 526 8495; fax: +1 208 526 2930.
E-mail addresses: robert@engr.ucsb.edu, robert.nourgaliev@inl.gov (R.R. Nourgaliev), theo@engr.ucsb.edu (T.G. Theofanous).

0021-9991/$ - see front matter
doi:10.1016/j.jcp.2006.10.031

itself, and we address issues of fidelity via higher grid resolution along with higher-order-accurate schemes, as made evident by Sethian [35], Osher and Fedkiw [29], Peng et al. [30], and others. More specifically, we will examine fidelity at the limits of grid resolutions, not only as expressed by mass conservation, but also by preservation of interfacial topologies, and by spurious, even if bounded, numerically-induced oscillations, as they could be damaging to the predictive capability we wish to attain.

These fidelity issues have been well known for some time (e.g., [32]), but were addressed effectively only very recently ([8,9,15] – see Table 1 for related work leading up to these). The approach [9] involves increasing the resolution through adaptive mesh refinement, implemented by means of the quad/octree-based algorithms, and incorporating particle-tracking features, implemented through Lagrangian markers "seeded" around the interface (PLS). As indicated in Table 1, with one exception all this work was done in the context of incompressible flow. For compressible flows, the structured adaptive mesh refinement (SAMR) is the preferred algorithm (to quad/octrees) [19], as spurious wave-reflections on interfaces of grids with different resolutions [7] are minimized. Furthermore, rather than marker particles, we thought it pertinent to examine the potential role of high order treatment for the advection operator. These two premises converge in suggesting the SAMR

Table 1
Works addressing the fidelity of the level set method[a]

Ref.	Year	Method	AMR	C/I	Order/scheme	Test problems	Coupled two-phase flow simulations
Mulder et al. [21]	1992	LS	–	C	2nd, ENO_2	–	Rayleigh–Taylor and Kelvin–Helmholtz instabilities
Sussman et al. [39]	1994	LS	–	I	2nd, ENO_2	–	Bubble rising; falling/colliding drops
Rider and Kothe [32]	1995	VOF, LS, MP	–	I	up to 4th, limited	ST and SBR, SVS, MVT2	–
Peng et al. [30]	1999	LS	–	I	up to 5th, $WENO_5$	ST and SBR	Volume-preserving mean curvature flow; motion with curvature dependent acceleration; 3D double bubble minimizer; incompressible vortex sheet
Strain [37]	1999	LS	Quad/ Octrees	I	2nd, unlimited	ST and SBR, SVS	–
Sussman et al. [41]	1999	LS	SAMR	I	2nd, ENO_2	–	Bubble(s) rising/merging; drop oscillation/ impact on water surface; collision of drops
Sussman and Puckett [42]	2000	Hybrid LS + VOF	SAMR	I	2nd, ENO_2	ST and SBR	Drop oscillation/impact on solid wall; capillary instability; bubble(s) rising
Enright et al. [8]	2002	Hybrid[b] LS + MP	–	I	up to 5th, $WENO_5$	ST and SBR, SVS MVT2, MVT3	Water poured into a cylindrical glass
Enright et al. [9]	2005	Hybrid LS + MP	Quad/ Octrees	I	up to 5th, $WENO_5$	ST and SBR, SVS MVT2, MVT3	–
Present		LS	SAMR	C/I	up to 11th, unlimited HOUC	ST and SBR, SVS MVT2, MVT3	Rayleigh–Taylor instability; shock-induced bubble collapse

The following notation is used: I: incompressible; C: compressible; VOF: volume of fluid; LS: level set; MP: marker particles; ST: simple translation; SBR: solid body rotation; SVS: single-vortex stretching; MVT2/3: 2/3D multiple-vortex tearing.

[a] Mass conservation of the level set method coupled with compressible fluid dynamics solvers is also discussed in [10,22].

[b] An application to solid mechanics is also available [43].

environment [2,26] – it provides us with simplicity to operate with as large a stencil as desirable, it is known to perform excellently in compressible flow [19], and it is convenient for parallelization.

The question of high order treatment requires further elaboration. As we can deduce from Table 1, current practice appears to have been limited to 5th order schemes, which, as well as all previous lower-order ones, were employed in conjunction with embedded limiting (non-linear weights assigned to constituent parabolas). The literature itself indicates that in this respect we have had a matter-of-fact choice that appears to be a remnant from gas dynamics, an area of application that these schemes were developed for, and have influenced in a major way [5,17]. What seems to have gone unnoticed is that such limiting, besides degrading the order of the level set discretization (e.g., accuracy of $WENO_5$ is actually between the 3rd and 5th orders), it is very expensive, and in fact not needed for the purposes here (interfacial kinematics). In particular, we will show that without any detriment to stability (demonstrated by von Neumann analysis for strong-stability-preserving Runge–Kutta time discretization), unlimited upstream central schemes can be pushed to the 11th order, without significant loss of efficiency in the overall computation, while performing at a level comparable to PLS.

More specifically, we numerically quantify the effect of increasingly higher order schemes, from the 3rd to 11th, and compare WENO (limited) vs. high-order upstream central (HOUC, unlimited) reconstructions of undivided differences in the Hamiltonian. Due to extremely low numerical dissipation, and ability to appropriately carry-on topological information within their large-stencil treatment, HOUC schemes appear to significantly improve the LS's ability to capture/preserve corners and other poorly-resolvable interface features. At the same time the Level Set's natural ability for numerical regularization with a proper vanishing viscosity solution is preserved.

The other key feature of our approach is the anchoring of the zero-level of the level set function during reinitialization, so as to eliminate drift in a stable and non-oscillatory fashion. Our approach capitalizes on the advantages of the PDE-based approach (high order, simple and parallelizable), without sharing the disadvantages (for our purposes here) of the fast marching (FM) method (low order, complex for parallelization). This anchoring is a finishing touch to Sussman et al. [41] whose approach remedied drift, but as we show in Section 4 could not eliminate spurious oscillations at the limits of grid resolution.

Following Rider and Kothe [32,33] and Enright et al. [8,9], fidelity of interface transport and reconstruction, and mass conservation are demonstrated on a number of benchmark problems, involving significant interfacial deformation, stretching, and tearing. These include translation of a thin filament, rotation and translation of a crusiform, rotation of the Zalesak disk, 2D convection/stretching in a single-vortex, 2D convection/stretching in a multiple-vortex, and 3D convection/stretching in a time-reversed double-vortex. All these tests involve uncoupled simulations with prescribed solenoidal velocity fields. In addition, we present fully-coupled flows (note that the compressible fluid dynamics is still treated using WENO schemes), including Rayleigh–Taylor instability (Mach □ 0), and shock-induced bubble collapse (Mach □ 1.7 in the liquid phase).

2. Discretization of Hamiltonian: high-order upstream central (HOUC) schemes

The level set (φ) equation [29,35] is a particular case of the more general Hamilton–Jacobi equation

$$\partial_t \varphi + H(\partial_j \varphi; \mathbf{r}) = 0; \tag{1}$$

where t, $\mathbf{r} = (x, y, z)$ and $H = |\nabla \varphi|$ are time, position vector and Hamiltonian, respectively. In general, the speed function F depends on $\mathbf{r}$ and first derivatives of φ, which makes Eq. (1) non-linear. For physical problems of concern here, the level set equation (1) can be reduced to the following simple advection form:

$$\partial_t \varphi + \mathbf{u} \cdot \nabla \varphi = 0 \tag{2}$$

by setting the speed function F to

$$F = \mathbf{u} \cdot \mathbf{n} \tag{3}$$

where $\mathbf{n} = \frac{\nabla \varphi}{|\nabla \varphi|}$ is the normal vector to the iso-levels, and $\mathbf{u} = (u, v, w)$ is the material velocity field, externally specified or available from a coupled fluid dynamics solver.

The consequence of this linear character of Eq. (2) is that instead of complex Riemann-solver-based techniques for treatment of the Hamiltonian [35], one can use the following simple upwinding:

Table 2
High-order upstream central (HOUC) schemes

Scheme	Undivided differences on the "left"[a], $D^{x;L}_{i;j;k}$	CFL stability limits $\mathfrak{C}$[b] for SSP-$RK_{3,3}$
UC_3	$\frac{1}{6}\varphi_{i-2;j;k} - \varphi_{i-1;j;k} + \frac{1}{2}\varphi_{i;j;k} + \frac{1}{3}\varphi_{i+1;j;k} + O(\Delta x^3)$	1.626
UC_5	$\frac{1}{60}(-2\varphi_{i-3;j;k} + 15\varphi_{i-2;j;k} - 60\varphi_{i-1;j;k} + 20\varphi_{i;j;k} + 30\varphi_{i+1;j;k} - 3\varphi_{i+2;j;k}) + O(\Delta x^5)$	1.435
UC_7	$\frac{1}{420}(3\varphi_{i-4;j;k} - 28\varphi_{i-3;j;k} + 126\varphi_{i-2;j;k} - 420\varphi_{i-1;j;k} + 105\varphi_{i;j;k} + 252\varphi_{i+1;j;k} - 42\varphi_{i+2;j;k} + 4\varphi_{i+3;j;k}) + O(\Delta x^7)$	1.244
UC_9	$-\frac{1}{630}\varphi_{i-5;j;k} + \frac{1}{56}\varphi_{i-4;j;k} - \frac{2}{21}\varphi_{i-3;j;k} + \frac{1}{3}\varphi_{i-2;j;k} - \varphi_{i-1;j;k} + \frac{1}{5}\varphi_{i;j;k} + \frac{2}{3}\varphi_{i+1;j;k} - \frac{1}{7}\varphi_{i+2;j;k} + \frac{1}{42}\varphi_{i+3;j;k} - \frac{1}{504}\varphi_{i+4;j;k} + O(\Delta x^9)$	1.127
UC_{11}	$\frac{1}{2772}\varphi_{i-6;j;k} - \frac{1}{210}\varphi_{i-5;j;k} + \frac{5}{168}\varphi_{i-4;j;k} - \frac{5}{42}\varphi_{i-3;j;k} + \frac{5}{14}\varphi_{i-2;j;k} - \varphi_{i-1;j;k} + \frac{1}{6}\varphi_{i;j;k} + \frac{5}{7}\varphi_{i+1;j;k} - \frac{5}{28}\varphi_{i+2;j;k} + \frac{5}{126}\varphi_{i+3;j;k} - \frac{47}{9240}\varphi_{i+4;j;k} - \frac{1}{2310}\varphi_{i+5;j;k} + O(\Delta x^{11})$	1.050

[a] HOUC interpolations on the "right" $D^{x;R}_{i;j;k}$ can be written similarly, applying stencil-symmetry; e.g., for UC_3 : $-\frac{1}{6}\varphi_{i+2;j;k} + \varphi_{i+1;j;k} - \frac{1}{2}\varphi_{i;j;k} - \frac{1}{3}\varphi_{i-1;j;k} + O(\Delta x^3)$.

[b] $\Delta t < \mathfrak{C}h/U_{max}$.

$$(uo_x\varphi)_{i;j;k} = \begin{cases} u_{i;j;k}\dfrac{D^{x;L}_{i;j;k}(\varphi)}{\Delta x} & \text{if } u_{i;j;k} > 0; \\ u_{i;j;k}\dfrac{D^{x;R}_{i;j;k}(\varphi)}{\Delta x} & \text{if } u_{i;j;k} < 0; \\ 0 & \text{otherwise} \end{cases} \tag{44}$$

(shown for x-direction only), where $D^{x;L=R}_{i;j;k}$ are undivided differences of the level set function at cell centers.

Moreover, since the level set is a smooth function, we have found that instead of traditionally used non-linear essentially non-oscillatory ($ENO_{2,3}$ or $WENO_5$) schemes [17,18,29,35], one can apply simple unlimited high-order upstream central (HOUC) discretization, without any detriment to numerical stability. That is, for present purposes, the HOUCs are both more efficient and more accurate than the WENO schemes.

Using Taylor series analysis, HOUC schemes were constructed up to 11th order and they are shown along with CFL stability limits (determined in the usual von Neumann manner with strong-stability-preserving (SSP) time discretization methods [13], and in particular with three-level, third-order Runge–Kutta SSP-$RK_{3,3}$ scheme [36]) in Table 2. We can thus appeal to Strang's theory [38] ensuring convergence as long as the appropriate CFL limit is observed [11,17]. It must be noted that even though the first derivatives of the level set function are discontinuous in the presence of corners, the HOUC schemes are sufficiently dissipative to slightly smear them out, ensuring thereby overall stability of the method.

3. Structured adaptive mesh refinement (SAMR): tagging and localization

The density of an Eulerian data structure can be cost-effectively increased using AMR. Here, we utilize the structured adaptive mesh refinement technology, developed by Berger and co-authors for hyperbolic conservation laws [2–4], and implemented as the SAMRAI library [16,34,44] at the Lawrence Livermore National Laboratory (LLNL).

Tagging. SAMR is based on a sequence of nested, logically rectangular meshes [2,24]. Tagging for refinement is a very important ingredient for building an effective SAMR hierarchy. The objective is to refine the grid around the interface, by first identifying all cells within the refinement corridor of radius ($\mathfrak{C}h$) (see Fig. 1 for definitions), and then collecting them into rectangular refinement patches, Fig. 2, using the point-clustering algorithm developed by Berger and Rigoutsos [4]. A simple way of doing this is to check for the change in sign of the level set function across two neighboring cells $_{(i,j,k)}$ and $_{(n)}$, in all grid-line directions, as delivered by the condition $(\varphi_{(i,j,k)}\varphi_{(n)}) \leqslant 0$. However, it is clear that this would miss subgrid scale features. To detect these, we need a better approximation of shape, and this is delivered by a non-linear fit in

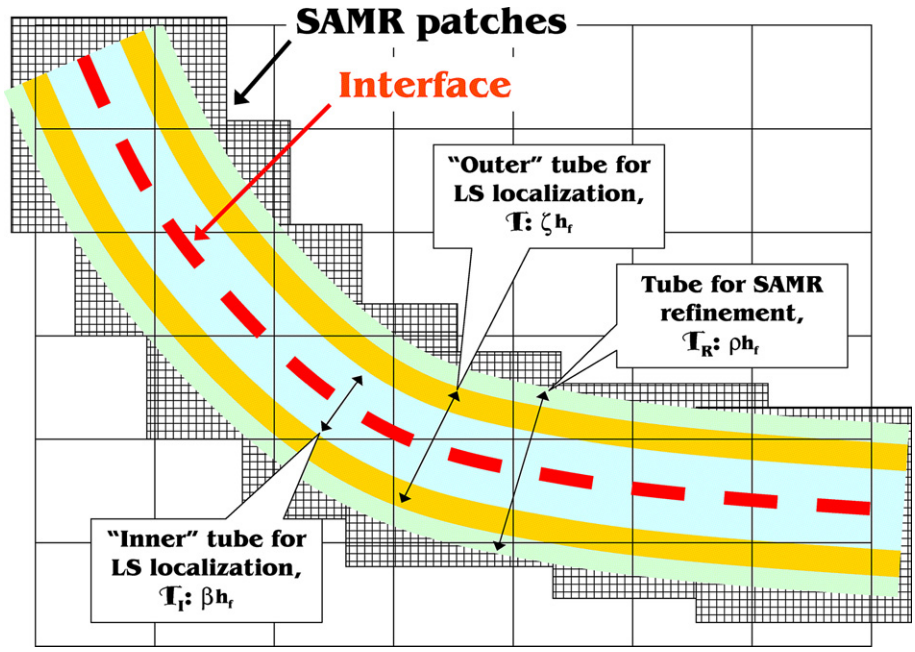

Fig. 1. Definition of the LS localization and AMR refinement tubes.

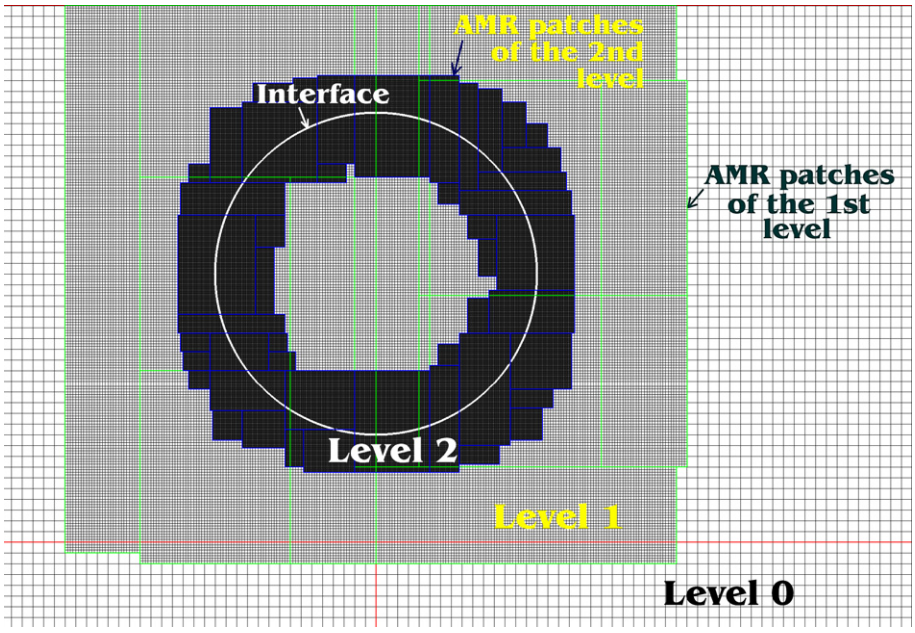

Fig. 2. Example of SAMR mesh with 3 levels of adaptation and refinement ratio 4.

every location and each grid-line direction. This we refer to as *non-linear tagging*. In implementation, these checks are performed only within a corridor around the interface ($.h$ in Fig. 1), and the non-linear step is employed only in cells where the linear tagging failed. A sample of the "linear tagging" failure and correspondent remedy by "non-linear tagging" is shown in Fig. 3.

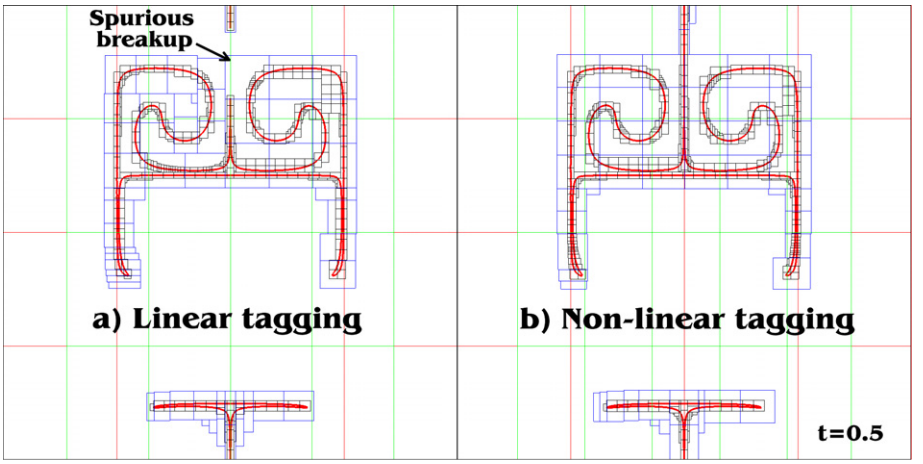

Fig. 3. Illustration of "spurious breakup" (a) and its elimination (b) for the "2D convection/stretching in a multiple-vortex" (see Problem #7 in Section 5.1.1). Zero level (in red) and SAMR patches. (For interpretation of the references to color in this figure legend, the reader is referred to the web version of this article.)

Localization. The efficiency of the level set method can be further improved by combining SAMR with Peng's et al. localization [30]. For this we need two additional localization tubes (Fig. 1). We solve the LS equation only within the "outer" tube $\mathfrak{T} = \{\mathbf{x} : |\varphi(\mathbf{x})| < \varsigma h\}$, where 1 and h are the radius of localization and the spacing of the computational mesh, respectively. The "inner" tube $\mathfrak{T}_1$ is needed so as to create a smooth transition from the actual, internal LS function to the external, cut-off values of it on either side. This transition occurs in the annular space between the "inner" and "outer" tubes. In implementation, we need to specify β and 1, as well as the "speed function vector". The latter is obtained from the material velocity as follows:

$$\mathbf{u}^{\mathrm{mod}} = \begin{cases} \mathbf{u} & \text{if } |\varphi| \leqslant \beta h; \\ \mathbf{u}\,\frac{2|\varphi|+h(\varsigma-3\beta)}{(\varsigma-\beta)^3 h^3}(|\varphi|-\varsigma h)^2 & \text{if } \beta h < |\varphi| \leqslant \varsigma h; \\ 0 & \text{if } |\varphi| > \varsigma h. \end{cases} \tag{5}$$

The radii β and 1 are set to $(s+1)$ and $(s+3)$, respectively, where s is the stencil of the spatial discretization scheme used.[1]

Localization is the key for our SAMR implementation. By setting $\varepsilon = s + 5$ we ensure that $1 < \varepsilon$. Thus by AMR-tagging the cells within a tube $\mathfrak{T}^R$ of the radius (εh_f), the LS treatment is fully confined within the top level of the SAMR hierarchy.

Communication of all SAMR levels is implemented through the "coarse-to-fine" prolongation and "fine-to-coarse" restriction operators, for which we employ third-order-accurate bi-cubic spline interpolations [31]. The algorithm is parallelized (MPI-based), distributing the solutions on different patches between different processors [16,34,44].

4. Reinitialization: anchoring the zero level

Due to discretization errors and the use of a cutoff function, Eq. (5), the level set tends to deviate from being a signed distance function, leading to the development of "steep" or/and "flat" regions and affecting the accuracy of the interface curvature computation. Moreover, left alone, when such steep/flat regions become excessive/extensive, small errors can result in spurious topological changes (appearance and disappearance of "islands", e.g. in the long tail of Fig. 4a). These errors can be prevented by using the "PDE-based-reinitialization" procedure[2] [30,39–41].

[1] Stencils s of UC_3, UC_5, UC_7, UC_9 and UC_{11} are 2, 3, 4, 5 and 6, respectively (see Table 2).

[2] Due to compatibility-with-SAMR issues [26], the "fast-marching-based-reinitialization" [1,35] is not an option here.

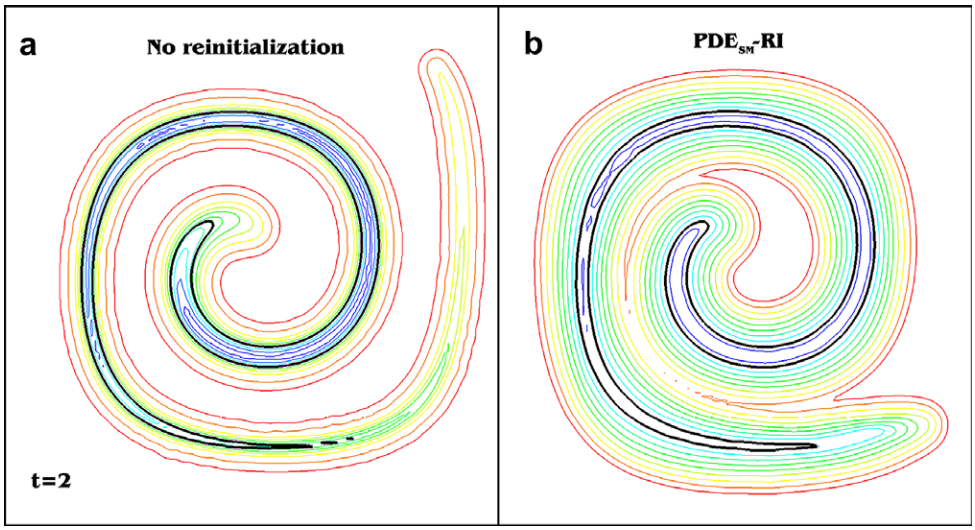

Fig. 4. The effect of reinitialization for the "2D convection/stretching in a single-vortex" (see Problem #6 in Section 5.1.1). (a) No reinitialization, (b) PDE_{SM}-based reinitialization (40 iterations applied every $Dt = 0.1$). SSP-$RK_{3,3}$/UC_7 and $WENO_7$ are applied for Level Set equation and reinitialization, respectively. Single-level grid with resolution 128^2. The cost of reinitialization is 28% more (CPU time), compared to the same run without reinitialization.

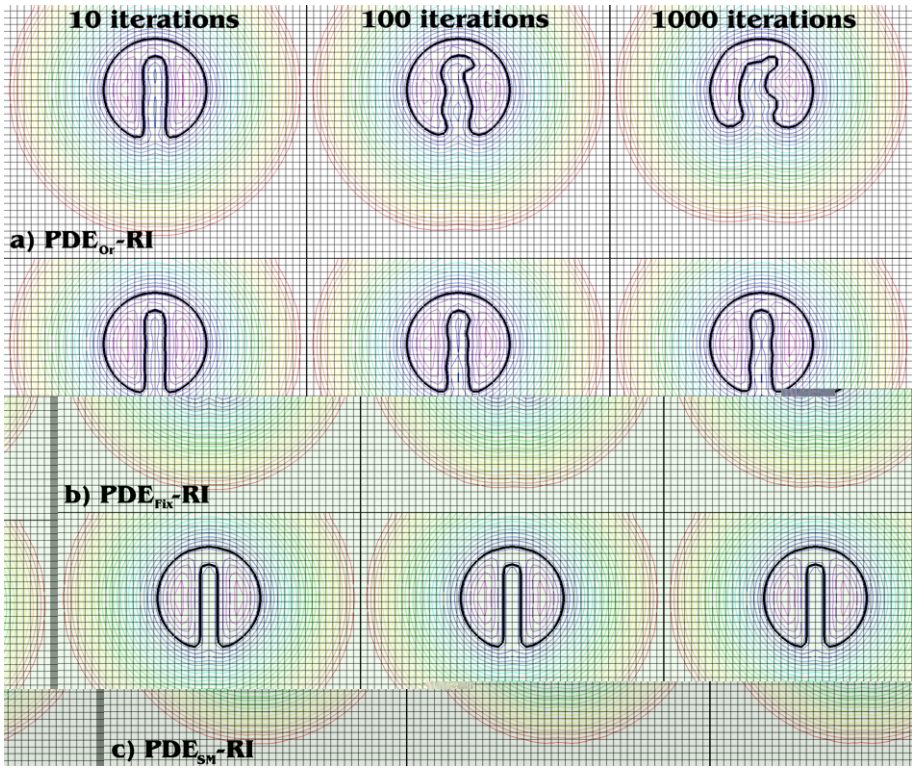

Fig. 5. Effect of reinitialization on interface position. 10, 100 and 1000 reinitialization steps are applied for re-distancing around a slotted disk. (a) Original Sussman's PDE-based reinitialization [39]. (b) Improved Sussman's PDE-based reinitialization [41]. (c) Present PDE_{SM}-based reinitialization. SSP-$RK_{3,3}$/$WENO_7$ scheme. Single-level grid with resolution 50^2.

The objective of this procedure is to "remold" the LS function so that it recovers its distance properties ($|\nabla\varphi| = 1$), without affecting the zero level. One way of doing so is by letting φ relax in pseudotime to steady-state, according to PDE equation (1) with the following Hamiltonian:

$$H = \mathcal{S}(|\nabla\varphi| - 1); \tag{6}$$

where $\mathcal{S}$ is some appropriate speed function that obtains zero value at the interface. The other general requirement on $\mathcal{S}$ is that it changes sign across the interface. It should be clear that at the limits of grid resolution, unless special precautions are taken, this procedure will move the interface ("drift") as in the original formulation [39], or it would prevent attainment of steady-state, as in the improved formulation [41]. As illustrated in Fig. 5, the latter eliminated the "drift", but "bounded oscillations" are still seen to exist.

To totally eliminate these oscillations we impose a special condition on $\mathcal{S}$, so that the zero level is truly and stably anchored on the interface. This is in addition to relieving the "drift" problem, also ensures reaching a steady-state where $|\nabla\varphi| = 1$. The details of implementation are listed below. As illustrated in Fig. 5, this anchoring provides further improvement in performance.

(a) At the beginning of each pseudo-time step, the speed functions $\mathcal{S}$ of all cells in the immediate neighborhood of the interface are computed minimizing the following "*attractor*" *function*:

$$F^{SM}_{MIN}(\mathcal{S}_{i,j,k}) = \sum_{m=1} \omega_m \left[\varphi^{n}_{i,j,k} + D\tau\mathcal{S}_{i,j,k}(1 - D|\nabla\varphi_{i,j,k}|) - \varphi^{\partial A}_{m|i,j,k}\right]; \tag{7}$$

where $D\tau$ is the pseudo-time step of the SSP-RK$_{3,3}$-based time advancement, and ω_m is the inverse-distance-based weight $\omega_m = \frac{[l=\mathrm{MAX}(10^{-8},\, d_m^2)]}{\sum_{l=1}^{N=\mathrm{MAX}(10^{-8},\, d_l^2)}}$ of the mth subcell marker in the neighborhood of the cell $_{(i,j,k)}$. The "support" dataset of N subcell markers is sampled within the "attraction radius" $d_m < 3h$, where $d_m = |\mathbf{x}_{i,j,k} - \mathbf{x}_m|$ and $\mathbf{x}$ denotes radius-vectors of the mth marker and cell $_{(i,j,k)}$. Minimization function Eq. (7) is designed so that the PDE-reinitialization-based update of the distance function $\varphi^{n+1}_{i,j,k}$ remains as close as possible to the *SM-based distance function* $\varphi^{\partial A}_{m|i,j,k}$. The latter one is formulated involving the following multi-dimensional Taylor expansion applied to the level set function in the neighborhood of the cell $_{(i,j,k)}$ and subcell marker $_{(m)}$:

$$\varphi^{\partial A}_{m|i,j,k} = (\mathbf{x}_{i,j,k} - \mathbf{x}_m)\cdot\mathbf{n}_{i,j,k} + \kappa(\varphi)_{i,j,k} + O(h^3): \tag{8}$$

Curvature terms $\kappa(\varphi)$ are necessary to maintain the formal third-order accuracy of the method and they are computed as (shown in 2D):

$$\kappa(\varphi) = \frac{1}{2}\left[(x_{i,j,k} - x_m)^2\sigma_x^2\varphi_{i,j,k} + (y_{i,j,k} - y_m)^2\sigma_y^2\varphi_{i,j,k} + 2(x_{i,j,k} - x_m)(y_{i,j,k} - y_m)\sigma_{xy}\varphi_{i,j,k}\right]: \tag{9}$$

To compute $\sigma_x^2\varphi_{i,j,k}$, $\sigma_y^2\varphi_{i,j,k}$ and $\sigma_{xy}\varphi_{i,j,k}$, we use the fourth-order-accurate central differences applied to the components of the normal vector $\mathbf{n} = \left(\frac{D^x}{D}; \frac{D^y}{D}\right)$. The "attractor" function equation (7) is minimized using parabolic interpolation and Brent's method [31]. Typically, this minimization procedure converges within 10–20 iterations to a tolerance of 10^{-9}.

(b) Then, the Hamiltonian H equation (6) is computed as suggested by Sussman et al. [39,41]:

$$H_{i,j,k} = \mathcal{S}_{i,j,k}(1 - D|\nabla\varphi_{i,j,k}|); \tag{10}$$

where $D|\nabla\varphi| = \sqrt{\left(\frac{D^x}{Dx}\right)^2 + \left(\frac{D^y}{Dy}\right)^2 + \left(\frac{D^z}{Dz}\right)^2}$ is dicretized using the following upwinding algorithm (shown for D^x only):

$$\begin{aligned} &\text{if } w_x^L > 0 \text{ and } w_x^L + w_x^R > 0 \;, && D^x = D^{x;L}_{i,j,k} \\ &\text{if } w_x^R < 0 \text{ and } w_x^L + w_x^R < 0 \;, && D^x = D^{x;R}_{i,j,k} \\ &\text{otherwise} \;, && D^x = 0 \end{aligned} \tag{11}$$

where $w_x^L = \mathcal{S}_{i,j,k}D^{x;L}_{i,j,k}$ and $w_x^R = \mathcal{S}_{i,j,k}D^{x;R}_{i,j,k}$

The undivided differences $D^{x,y,z}$ at cell centers are reconstructed with WENO$_N$, where N is chosen to be consistent with the order of discretization of the level set equation (2).

Our experience is consistent with what is already known – a few reinitialization steps at each physical time step are sufficient to condition the LS function, so that complete reinitialization to near steady-state is only needed once in awhile (typically, every 20–100 physical time steps). We actually employ these few steps only in the annular portion of the corridor, which also saves in computation effort of the minimization problem, Eq. (7).

In regards to costs, the following summarizes our experience: (a) the most expensive part is the computation of the Hamiltonian, especially since we found it is necessary, as do others, to use (non-linear) WENO[3]; (b) the cost of the minimization step is by comparison limited, as it is only needed within one cell on either side of the interface, while the Hamiltonian needs to be computed everywhere inside the "outer" tube; (c) as a specific example, the cost of our procedure applied to Problem #6 (see Section 5.1.1 and Fig. 4) is 20% more compared to [41].

5. Numerical examples

We will consider two groups of numerical examples. In the *first group*, the velocity field is prescribed. The areas of concern for judging success of the interface kinematics treatment include (i) the method's ability to faithfully capture poorly-resolved interface structures, such as thin elongated filaments and corners; (ii) high-order grid convergence; (iii) mass conservation; and (iv) efficiency of computations. We will consider not only problems with stationary shapes of interface (i.e., simple translations and solid-body rotations), but also those involving continuously refining length scales (interface stretching, tearing, severe deformation and fragmentation). The focus is placed on performance at the limit of grid resolution (1–3 nodes per interfacial topological features), as practical problems of interest here are *multiscale multiphase flows* with evolving, continuously refining length scales (e.g., Rayleigh–Taylor mixing, bubble collapse and drop fragmentation). Considering that in 3D the actual cost of doubling grid resolution is (×16), all gains made in pushing the limits of grid resolution are of enabling significance. We consider a wide spectrum of numerical tests, including all those known from past work, as well as embellishments on them, such as the combined rotation/translation of a "crusiform".

Numerical examples of the *second group* involve full coupling of interface kinematics with the dynamics of the two fluids, and these are chosen to range from incompressible flow (Rayleigh–Taylor mixing) to highly compressed states in two fluids of great acoustic impedance mismatch (shock-induced bubble collapse).

In all simulations presented here, we apply second-order extrapolations as boundary conditions for the level set equation. For computation of mass in two dimensions, we use a second-order-accurate algorithm. In particular, we first find subcell positions of the interface as the cut points of zero level with gridlines, and then piecewise-linearly reconstruct the subcell area as a collection of polygons, using the subcell cut points as their vertices. In three dimensions, the volume is computed using the first-order algorithm as described by Enright et al. in [8].

AMR calculations will be denoted as $\mathrm{SAMR}_{C}^{A=B}$, where A is the grid refinement ratio between levels of adaptation in a hierarchy of SAMR grids, B is the total number of levels in a hierarchy, and C is the effective grid resolution or grid size if corresponding uniform grids were to be applied over the whole domain.

The following parameters are used for SAMR grid generation: (1) the Berger and Rigoutsos's point-clustering algorithm [4] is applied (using a binary tree communication with hand-coded sends and receives); (2) the efficiency tolerance (i.e., a threshold value for the percentage of tagged cells in each SAMR box) is set to 90%; (3) the combine tolerance (i.e., a threshold value for the sum of the volumes of two boxes into which a box may be potentially split) is specified at 80%. More detail explanation of these parameters can be found in [34].

5.1. Fidelity tests for interface kinematics

Following a description of all problems considered (including illustrations of the type of under-resolution failures involved), we present and discuss the results by focusing on a succession of issues as follows: (a) the role of limiters, (b) the role of discretization order and grid convergence, and (c) the role of AMR and

[3] PDE-reinitialization equation (1) is non-linear. Therefore, unlimited HOUC interpolations are unstable.

Table 3
Descriptions of numerical problems

#	Domain	Velocity field	Initial shape/location	Duration (t_{end})
I. Solid-body translation/rotation				
1	2	$u = 1$	A thin filament of thickness $h = 0.0125$ at $x = 0.5$.	1
2	100×100	$u = \frac{\pi}{314}(50 - y)$ $v = \frac{\pi}{314}(x - 50)$	A slotted disk of radius 15 at $\mathbf{x} = (50; 75)$. The width and length of the slot are 5 and 25, respectively.	628 One solid-body revolution by $t = 628$ (Fig. 6)
3	1×1	$u = \pi(0.3 - y + 0.4t(-0.4))$ $v = \pi(0.7 - x + 0.4t + 0.4)$	A "crusiform" of width $h = 0.02$ and length scale $L = 0.2$ at $\mathbf{x} = (0.7; 0.3)$ and tilted on 45°.	1 A full rotation and translation left-upwards by $t = \frac{2}{5}\frac{2}{2}$ (Fig. 7)
II. Moderate interface deformation, tearing and stretching				
4	1×1	$u = -2\cos(\frac{\pi t}{T})\cos(\pi y)\sin^2(\pi x)\sin(\pi y)$ $v = 2\cos(\frac{\pi t}{T})\cos(\pi x)\sin^2(\pi y)\sin(\pi x)$	A circle of radius $\frac{3}{20}$ at $\mathbf{x} = (\frac{1}{2}; \frac{3}{4})$.	$T = 2$ and 8 One period of circle's stretching and compression (Fig. 8)
5	$1 \times 1 \times 1$	$u = 2\cos(\frac{\pi t}{3})\sin^2(\pi x)\sin(2\pi y)\sin(2\pi z)$ $v = -\cos(\frac{\pi t}{3})\sin^2(\pi y)\sin(2\pi x)\sin(2\pi z)$ $w = -\cos(\frac{\pi t}{3})\sin^2(\pi z)\sin(2\pi x)\sin(2\pi y)$ (See streamlines in Fig: 9a)	A sphere of radius $\frac{3}{20}$ at $\mathbf{x} = (\frac{1}{2}; \frac{3}{4})$.	3 One period of sphere's stretching and compression (Fig. 9)
III. Severe (ultimately unresolvable) interface deformation, tearing and stretching				
6	1×1	$u = -2\cos(\pi y)\sin^2(\pi x)\sin(\pi y)$ $v = 2\cos(\pi x)\sin^2(\pi y)\sin(\pi x)$	A circle of radius $\frac{3}{20}$ at $\mathbf{x} = (\frac{1}{2}; \frac{3}{4})$.	5 Approximately 4.5 rings of the spiral (Fig. 10)
7	1×1	$u = \sin(4\pi x - \frac{1}{2})\sin(4\pi y - \frac{1}{2})$ $v = \cos(4\pi x - \frac{1}{2})\cos(4\pi y - \frac{1}{2})$ (See Fig:11)	A circle of radius $\frac{3}{20}$ at $\mathbf{x} = (\frac{1}{2}; \frac{3}{4})$.	1 Severe deformation of a circle (Figs. 12 and 13)
8	1×1	$u = \cos(\pi t)\sin(4\pi x - \frac{1}{2})\sin(4\pi y - \frac{1}{2})$ $v = \cos(\pi t)\cos(4\pi x - \frac{1}{2})\cos(4\pi y - \frac{1}{2})$	A circle of radius $\frac{3}{20}$ at $\mathbf{x} = (\frac{1}{2}; \frac{3}{4})$.	2 One period of severe circle's stretching and compression

All velocity fields are solenoidal.

comparison with PLS. Having established in (a) the value of unlimited HOUCs, items (b) and (c) are considered only in terms of them.

5.1.1. Problems considered

Descriptions of the eight test-problems considered are provided in Table 3. As indicated, they belong to three subgroups.

Those in *Subgroup I* (Problems #1–3) involve solid-body rotations and translations. In particular, we consider translation of a thin filament (Problem #1); solid-body rotation of "Zalesak disk" [47], Fig. 6 (Problem #2); and combined rotation/translation of a "crusiform", Fig. 7 (Problem #3). Problem #3 is introduced here, as we found it to be more capability-straining than the "Zalesak disk" test [47].

In the problems of *Subgroup II* (#4 and #5) the interface is subjected to moderate (resolvable) tearing, stretching and deformation. The "2D convection/stretching in a time-reversed single-vortex" (Problem #4, Fig. 8) was originally introduced in [33]. It involves periodical stretching/compression of a circle, forcing the interface to return to its original circular shape at the end of each cycle. Somewhat similar is Problem #5, Fig. 9 ("3D convection/stretching in a time-reversed double-vortex"), introduced in [8]. Here, the sphere

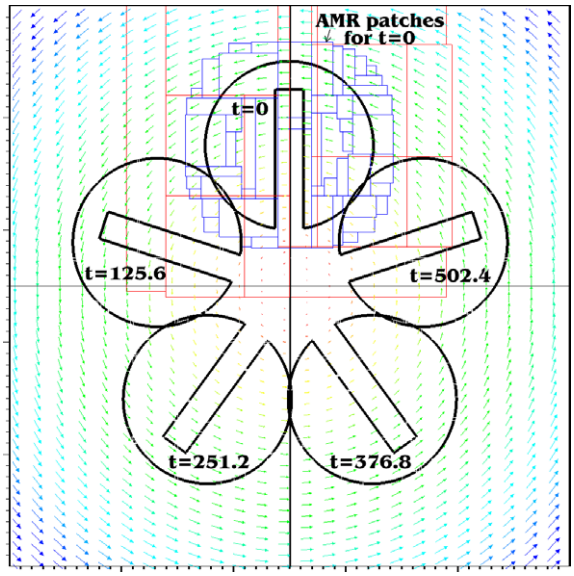

Fig. 6. Illustration of one rotation of the "Zalesak disk" (Problem #2). SSP-RK$_{3,3}$/UC$_7$ scheme on SAMR$^{4=3}_{1600^2}$.

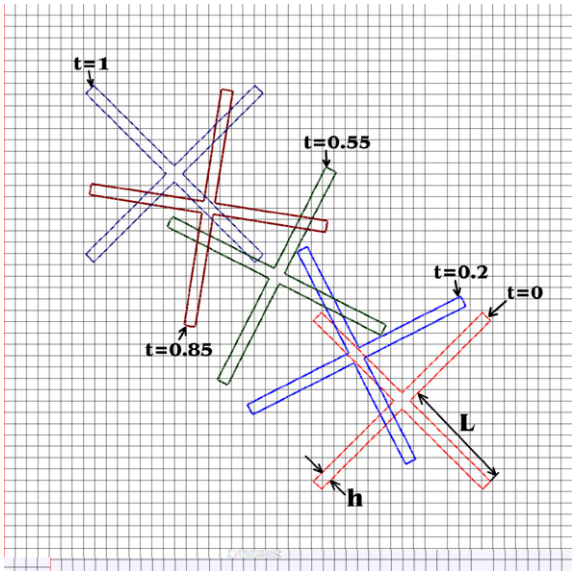

Fig. 7. Trajectory of the rotating and translating "crusiform" (Problem #3). SSP-RK$_{3,3}$/UC$_{11}$ scheme on SAMR$^{4=3}_{800^2}$.

is entrained by two rotating vortices, which tear the sphere apart, creating a pancake-like structure by the time of maximum deformation $t = 1.5$. At the end of each cycle, the interface should return to its original spherical shape and Fig. 9 illustrates how it may fail to do so when under-resolved.

The most challenging problems belong to *Subgroup III* (Problems #6, #7 and #8), which is characterized by continuously refining length scales, and the interface subjected to extreme (ultimately unresolvable) tearing, stretching and deformation. Problem #6 ("2D convection/stretching in a single-vortex"), introduced in [33], involves a circle stretched into a long spiral filament by a single-vortex. By time $t = 5$, there are approximately 4.5 rings in the spiral, Fig. 10. With continuing stretching, the spiral filament becomes thinner and thinner. Problems #7 and #8 ("2D convection/stretching in a multiple-vortex") involve deformation of a circular body in very complex velocity field (Fig. 11). By the time of maximum deformation, the major fraction of the circle is entrained into the two nearest (left and right) vortices, while the rest (smaller portion) is

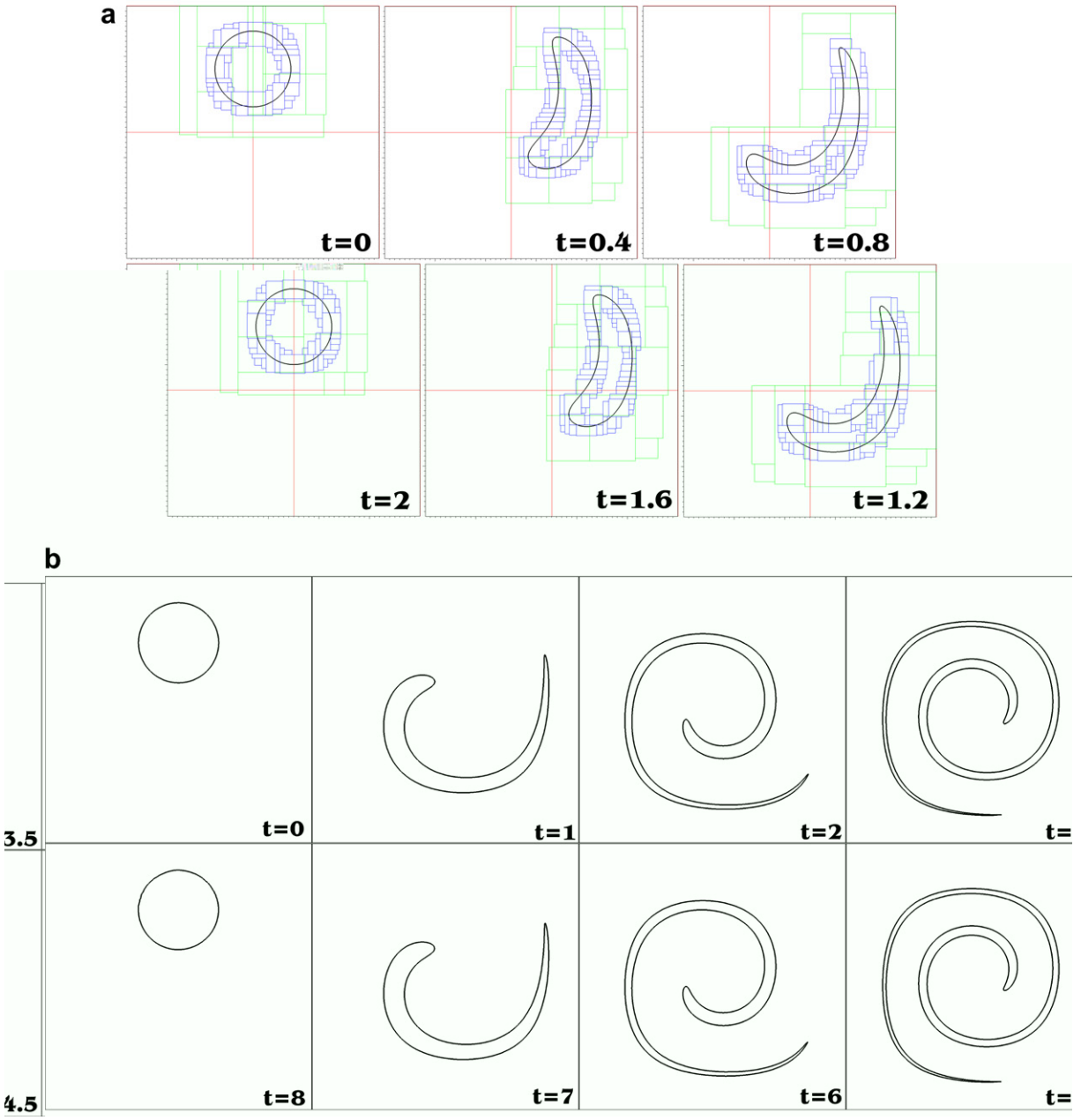

Fig. 8. "2D convection/stretching in a time-reversed single-vortex" (Problem #4). Top: Evolution of interfacial shape and AMR patches for $T=2$ (SSP-RK$_{3,3}$/UC$_7$ scheme on SAMR$^{4=3}_{1600^2}$). Bottom: Evolution of interfacial shape for $T=8$ (SSP-RK$_{3,3}$/UC$_{11}$ scheme on SAMR$^{2=3}_{512^2}$).

entrapped as thin filaments by other four nearest vortices, see Figs. 12 and 13. In difference to Problem #7, Problem #8 is set to be oscillatory (time-reversed), forcing the circle to return to its original shape by the end of each cycle.

5.1.2. The role of limiting

Illustrative comparisons of HOUC (unlimited) and WENO (limited) schemes for Problems #2, 3, 4 and #6 are presented in Figs. 14–16 and 22a. The global message is conveyed by Table 4, which demonstrates superior mass conservation properties of HOUCs.

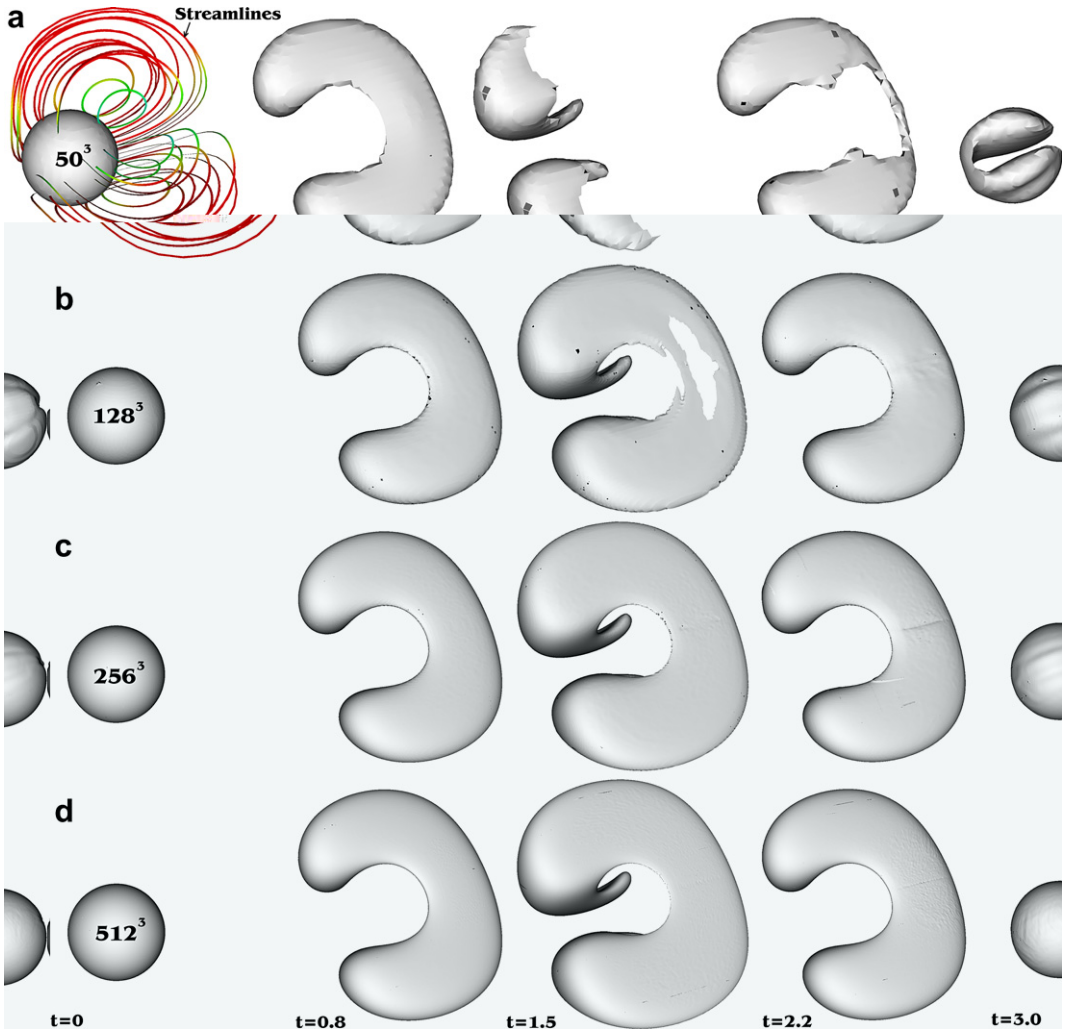

Fig. 9. Evolution of interfacial shape for one cycle of the "3D convection/stretching in a time-reversed double-vortex" (Problem #5). SSP-$RK_{3,3}/UC_7$ scheme. Solution with grids: (a) 50^3, (b) $SAMR^{2=2}_{128^3}$, (c) $SAMR^{2=3}_{256^3}$ and (d) $SAMR^{2=4}_{512^3}$.

Evidently, HOUC schemes are able to capture fine interface topological features significantly better than WENOs. The case of "Zalesak disk" with grid resolution of 2.5 nodes per slot's width is illustrated in Fig. 14. After one revolution, the $WENO_5$ smears the slot severely. With UC_5, the corners of the slot are resolved significantly better. By increasing the accuracy of discretization to the seventh order, the performance of WENO is significantly improved, becoming comparable to the UC_5, but still inferior to the UC_7. More significant detrimental effects of limiting are observed for the rotating and translating "crusiform", Fig. 15. In this case, under a grid of two nodes per branch width, the $WENO_5$ resulted in a complete disappearance of the "crusiform". Significant smearing occurs also for the $WENO_7$. With HOUC, the fidelity of interface kinematics is significantly higher, allowing to maintain high resolution of thin filaments and corners. For this problem, the UC_5 performed significantly better than $WENO_7$, Fig. 15. The same detrimental effects of limitings are also recorded for interface stretching flows, shown as an example in Fig. 16, at the stage when the grid provides two computational nodes over the filament width.

The generally poor performance of limiting at the limits of grid resolution is due to effective reduction of the discretization order of the WENO interpolation. The Nth-order-accurate $WENO_N$ reconstruction scheme for cell-centered discrete undivided differences $D^{x;L=R}_{i;j;k}$ is a combination of $n¼\frac{Nþ1}{2}$, nth-order polynomials:

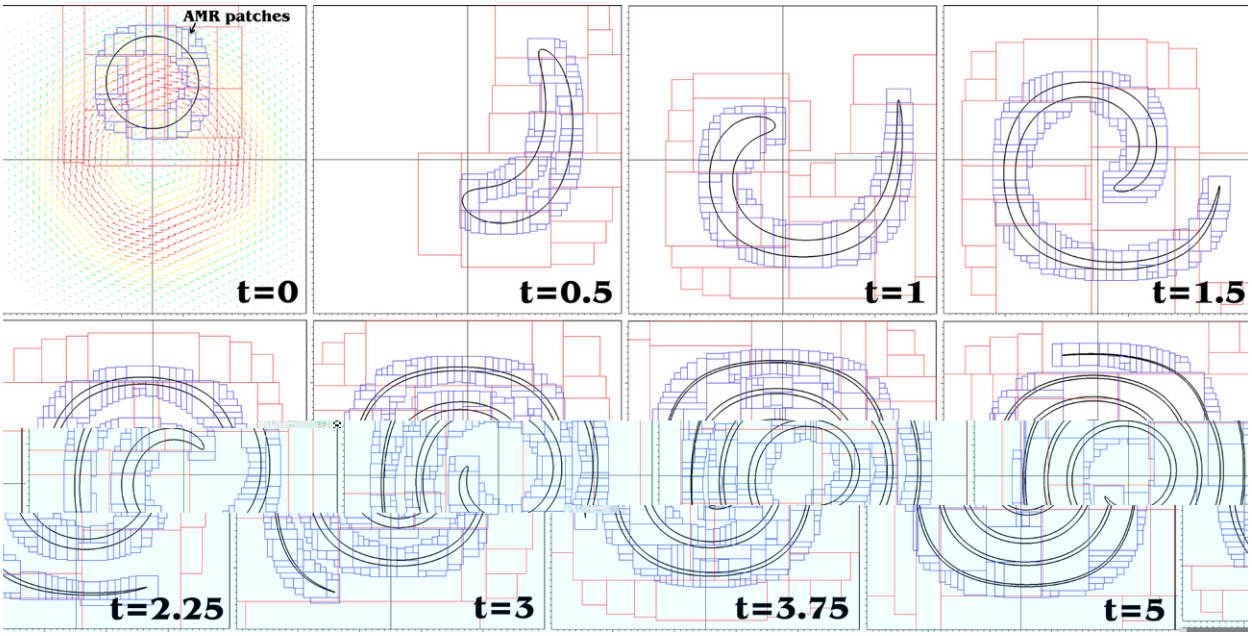

Fig. 10. Evolution of interfacial shape and AMR patches for the "2D convection/stretching in a single-vortex" (Problem #6). SSP-RK$_{3,3}$/UC$_7$ scheme on $\mathrm{SAMR}^{4=3}_{1600^2}$.

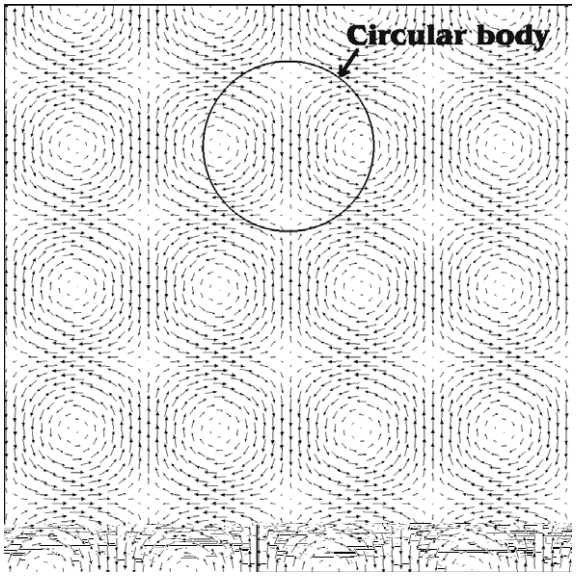

Fig. 11. Velocity field for the "2D convection/stretching in a multiple-vortex" (Problems #7 and #8).

$$P_{\mathrm{WENO_N}}(x) = \sum_{k=0}^{n-1} \varpi_k^{(n)} P_k^{(n)}(x) \tag{12}$$

where $\varpi_k^{(n)}$ are non-linear weights:

$$\varpi_k^{(n)} = \frac{\alpha_k^{(n)}}{\alpha_0^{(n)} + \cdots + \alpha_{n-1}^{(n)}}; \quad \text{and} \quad \alpha_k^{(n)} = \frac{C_k^{(n)}}{(10^{-10} + \mathrm{IS}_k^{(n)})^2} \tag{13}$$

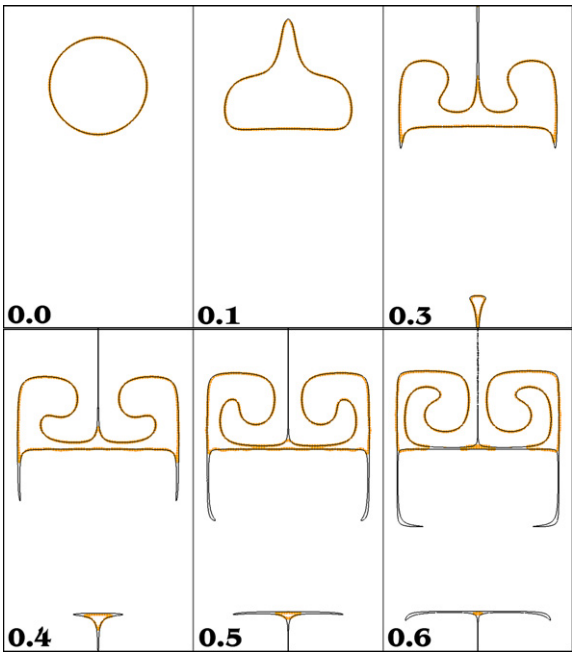

Fig. 12. Evolution of interfacial shape for the "2D convection/stretching in a multiple-vortex" (Problem #7). SSP-$RK_{3,3}/UC_7$ scheme. Orange thick dashed line: uniform 128^2 grid. Black thin solid line: $SAMR^{4=4}_{8192^2}$.

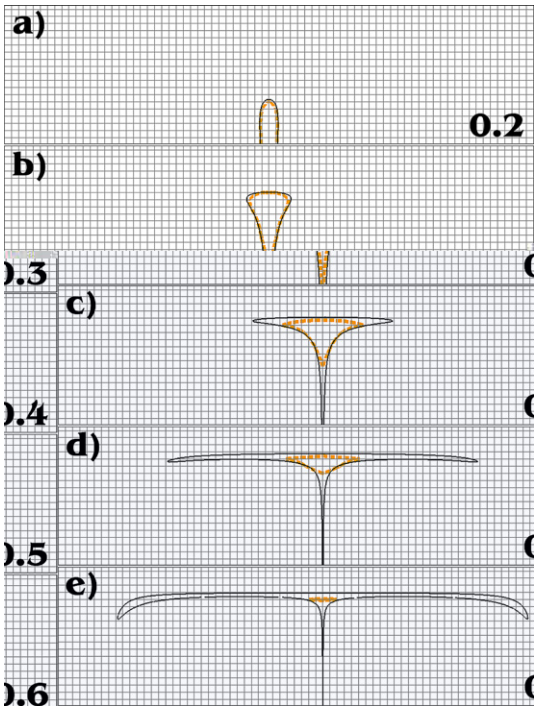

Fig. 13. A closer look at the poorly-resolved filaments entrained into the four nearest vortices located below, for the "2D convection/stretching in a multiple-vortex" (Problem #7), and illustration of failure when under-resolved. SSP-$RK_{3,3}/UC_7$ scheme. Orange thick dashed line: uniform 128^2 grid. Black thin solid line: $SAMR^{4=4}_{8192^2}$. As a background, the computational mesh at resolution 128^2 is also shown.

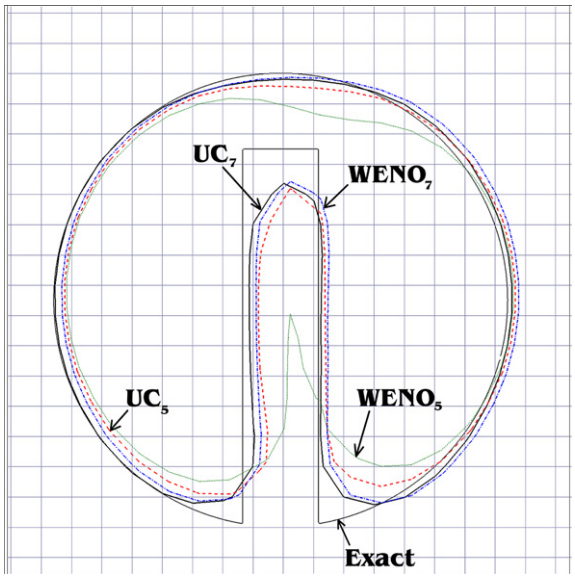

Fig. 14. The effect of non-linear weights on resolution in corners and slot after one rotation of the "Zalesak disk" (Problem #2). Grid is set at 2.5 nodes per slot width (50^2).

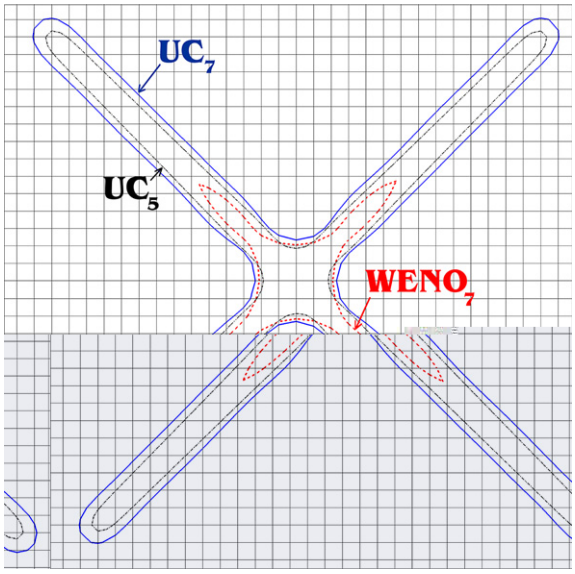

Fig. 15. The effect of non-linear weights on resolution of the crusiform (Problem #3). Grid is set at two nodes per branch width (100^2).

designed to "catch" discontinuities of the interpolated function[4] and "essentially eliminate" oscillations associated with them [5]. It is easy to demonstrate that, with "optimal" weights $\varpi_k^{\eth np} \frac{1}{4} C_k^{\eth np}$, reconstructions according to Eq. (12) are identical to HOUC schemes (Table 2), and this is why these schemes were denoted as "Linear WENO" (LWENO) in our previous studies [24–26]. Smoothness estimators $IS_k^{\eth np}$ for WENO schemes up to 11th-order are developed by Jiang and Shu [17] and Balsara and Shu [5]. As a consequence, greater weights are assigned to WENO's constituent polynomials located further from the interface. By doing this,

[4] As discussed in Section 2, the level set is a continuous function, making this kind of limiting unnecessary.

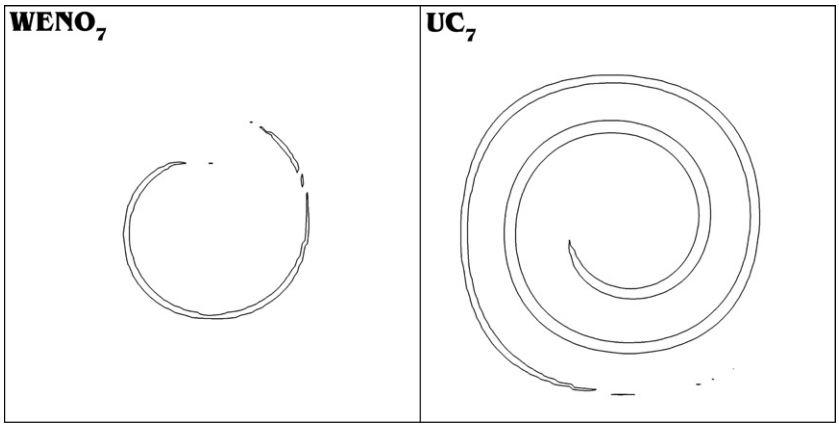

Fig. 16. The effect of non-linear weights on resolution of thin interface structures in the "2D convection/stretching in a single-vortex" (Problem #6). $WENO_7$ scheme vs. UC_7, using grid 100^2. $t = 2$. There are 2 nodes per filament width at this stage.

Table 4
Effect of limiting on mass conservation

# Problem	Grid resolution	Scheme	Error
2	50^2	$WENO_5$	7%
		UC_5	**3.2**%
3	1 node/*h*	$WENO_5$	100%
		$WENO_7$	100%
		UC_5	**86.9**%
		UC_7	**56.1**%
	2 nodes/*h*	$WENO_5$	100%
		$WENO_7$	81.8%
		UC_5	**4.05**%
		UC_7	**1.76**%
	4 nodes/*h*	$WENO_5$	5.5%
		$WENO_7$	4.07%
		UC_5	**2.63**%
		UC_7	**1.5**%

extra numerical diffusion is introduced – so that in practice the accuracy of WENO schemes is always between *n*th and *N*th order.

This is demonstrated in Fig. 17, which shows spatial distribution of non-linear weights of $WENO_5$ for numerical example 1. In particular, upstream from the filament, the weight of the right (downstream) polynomial is essentially reduced to zero, putting the greater weight to the left (downstream) polynomial, effectively reducing the stencil of the scheme and actual accuracy of discretization. Clearly, these non-linear weights having been developed for discontinuous functions (designed for capturing shocks and contacts in hyperbolic conservation laws), end up behaving inappropriately when applied to smooth function such as the LS.

Furthermore, non-linear WENO schemes are expensive, as the computation of the smoothness estimators $IS_k^{\hat{\partial}\hat{n}\hat{p}}$ and non-linear weights, Eq. (13), leads to approximately 50% increase in computational time for $WENO_5$ (more at higher order). As a result, even the most expensive 11th-order UC is comparable to $WENO_5$ and approximately 30% faster than $WENO_7$.

5.1.3. The role of discretization order and grid convergence

The effects of accuracy of HOUC schemes and grid convergence are shown in Figs. 18–22a. Evidently, with increasing the order of dicretization, from the 3rd- to the 11th-, resolution of thin filaments and other fine-grain interface structures improved significantly. Correspondingly, mass conservation errors become smaller (Table 5).

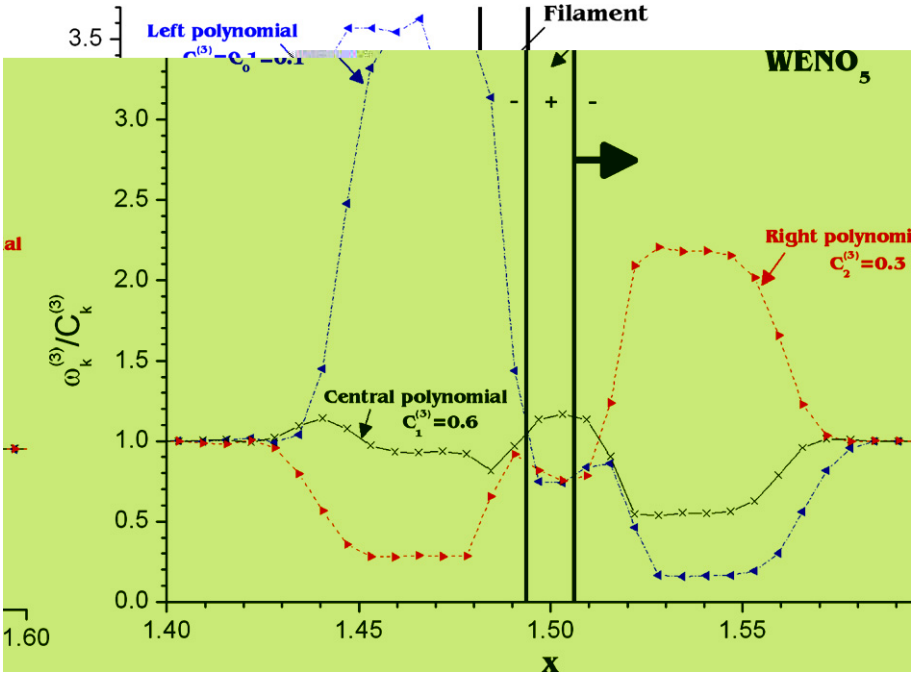

Fig. 17. Spatial distribution of non-linear weights for $WENO_5$ scheme, applied for Problem #1. Grid resolution is 2 nodes per h.

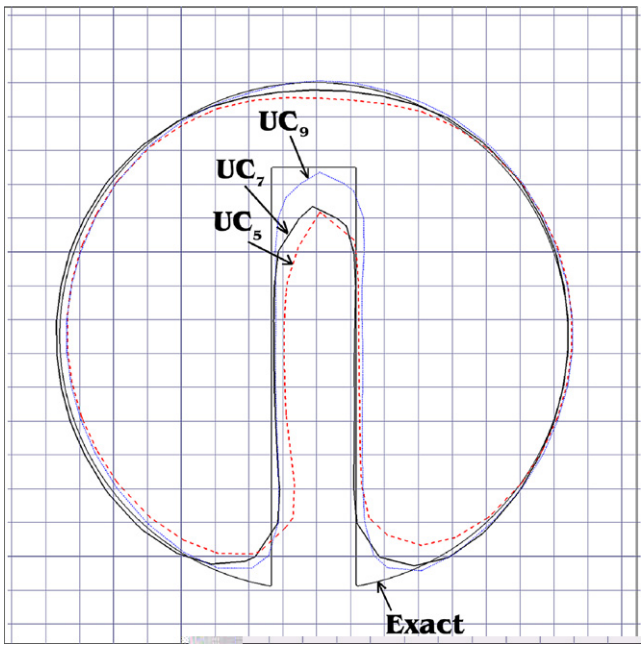

Fig. 18. The effect of accuracy of discretization scheme on resolution of corners and slot after one rotation of the "Zalesak disk" (Problem #2). Grid is set at 2.5 nodes per slot width (50^2).

As one can see from Fig. 21, all schemes converge with the rate between the first and second order. This is because derivatives of the exact level set function are discontinuous (at the centers of the filament, problem #1; and corners of the "crusiform", problem #3), which imposes first-order truncation errors for interface normals. The HOUC treatment is nevertheless stable, as the "corner-capturing" features of the level set method

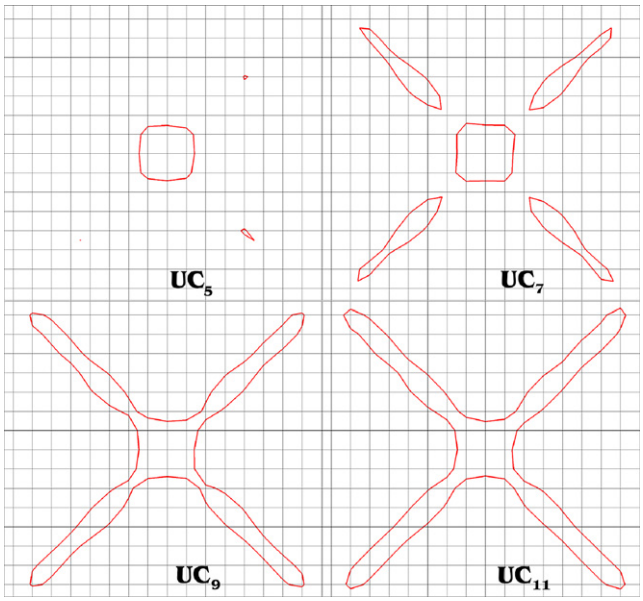

Fig. 19. The effect of accuracy of discretization scheme on resolution of the "crusiform" (Problem #3) after t ¼ $2\frac{p}{2}$. Grid is set at one node per branch width (50^2).

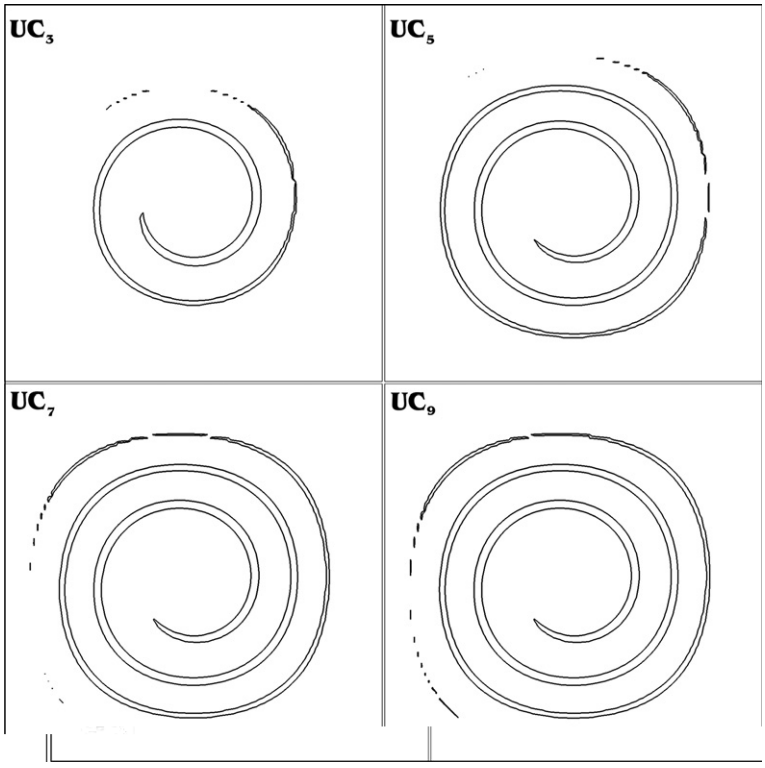

Fig. 20. The effect of discretization order (HOUC) on resolution of thin interface structures in the "2D convection/stretching in a single-vortex" (Problem #6). $t = 5$. Grid is set at 1–2 nodes per filament width (128^2).

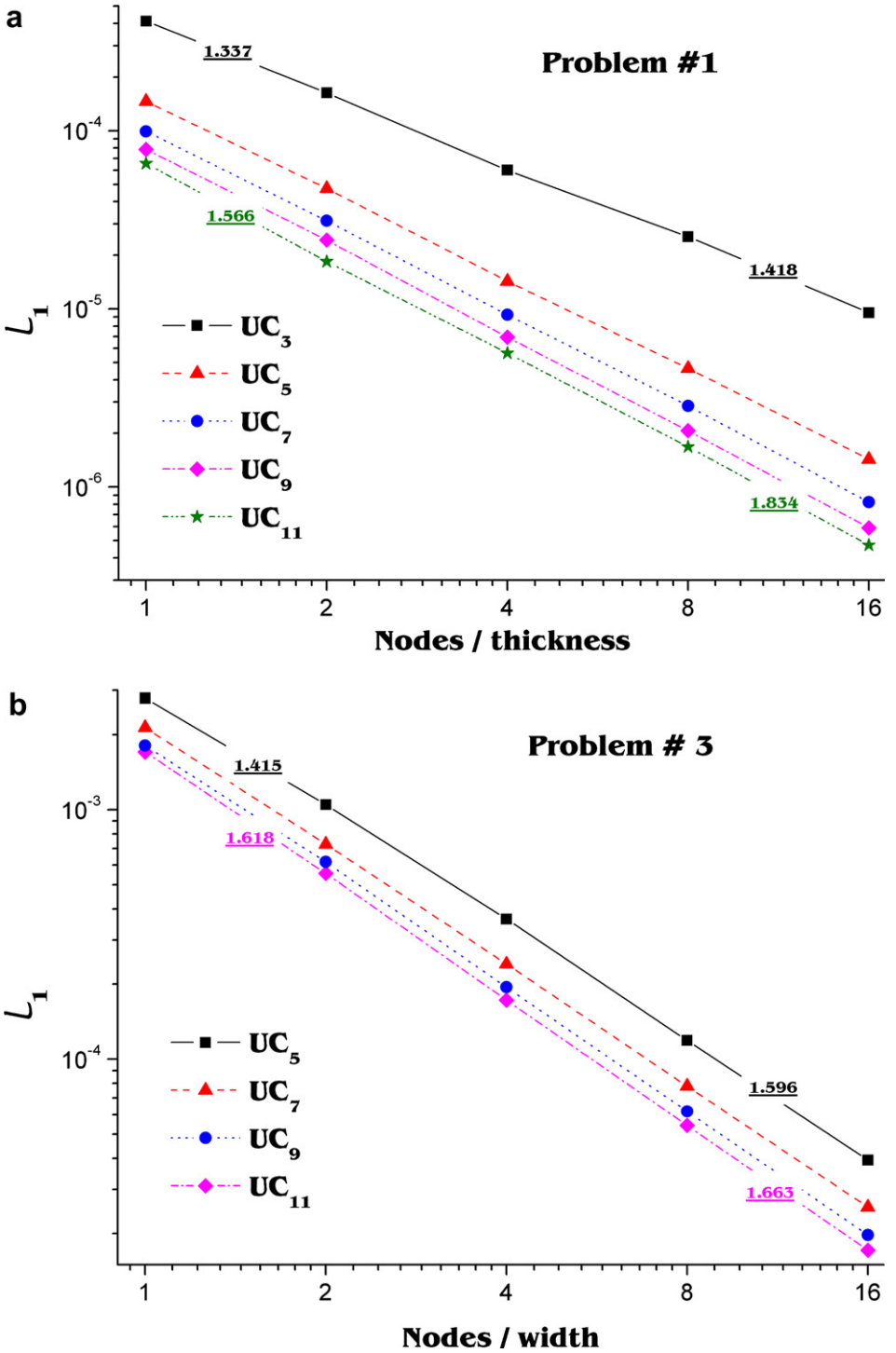

Fig. 21. Grid convergence of HOUC schemes for Problems #1 (a) and #3 (b), expressed in terms of L_1-norm of the error for the level set. Convergence rates for UC_3, UC_5 and UC_{11} are also shown for grid intervals ($1 \rightsquigarrow 2$) and ($8 \rightsquigarrow 16$) nodes/h.

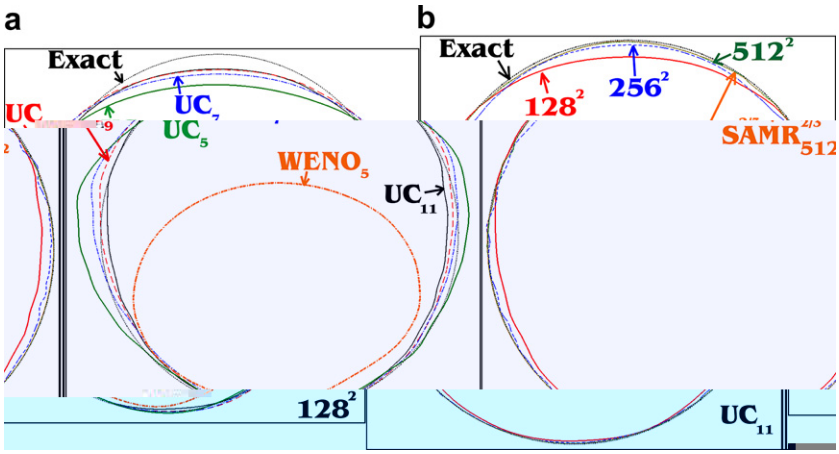

Fig. 22. Final shape of interface for Problem #4 with $T = 8$. (a) The effect of discretization order (HOUC). (b) Grid convergence of UC_{11} scheme (uniform-grid-512^2 and $SAMR^{2=3}_{512^2}$ solutions are nearly identical).

Table 5
Effect of discretization order and grid convergence on mass conservation

# Problem	Grid resolution	Scheme	Error
2	50^2	UC_5	3.2%
		UC_7	1.1%
	100^2	UC_5	1.44%
		UC_7	0.8%
	200^2	UC_7	0.16%
3	1 node/h	UC_5	86.9%
		UC_7	56.1%
		UC_9	31%
		UC_{11}	27.2%
	2 nodes/h	UC_5	4.05%
		UC_7	1.76%
		UC_9	0.58%
		UC_{11}	0.23%
	4 nodes/h	UC_5	2.63%
		UC_7	1.5%
		UC_9	0.4%
		UC_{11}	0.15%
6	128^2	UC_5	8.04%
		UC_7	5.14%
		UC_9	4.05%
	256^2	UC_7	3.08%
	$SAMR^{4=3}_{1600^2}$	UC_7	0.33%

are embedded through the "numerical smearing/surface tension" of the Eulerian treatment, providing a sufficient numerical regularization with a proper vanishing-viscosity-solution, see Fig. 23. Even though all tested numerical schemes converge with the rate between the first and second order, higher-order treatment exhibits significantly lower discretization errors (Fig. 21).

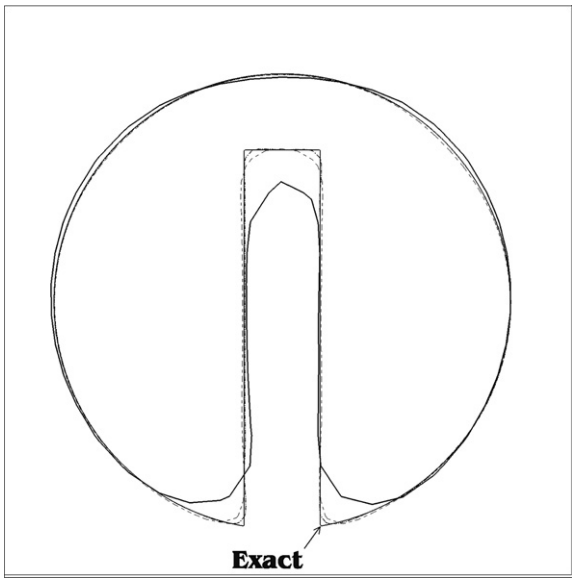

Fig. 23. Grid convergence of UC_7 scheme. Interface after one rotation of the "Zalesak disk" (Problem #2). Computational grids are: 50^2 (thick solid line), 100^2 (thin dashed line), 200^2 (thin dash-dot line) and 1600^2 (thin solid line, indistinguishable from the exact).

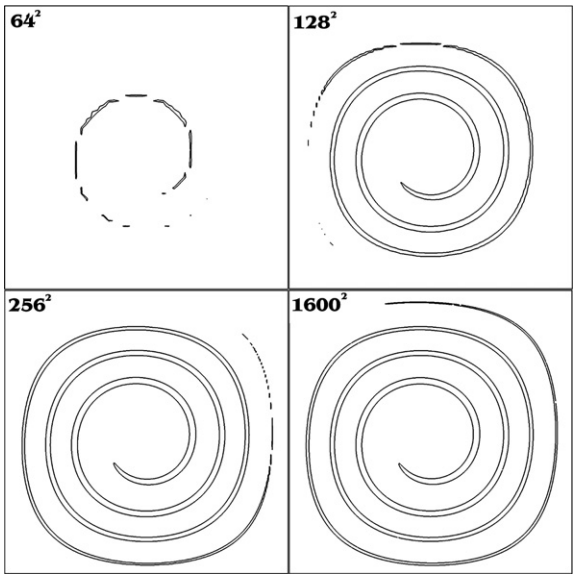

Fig. 24. Grid convergence of UC_7 for the "2D convection/stretching in a single-vortex" (Problem #6). $t = 5$. The effective resolution 1600^2 is by AMR.

It is understood that the introduced here improvement of the LS treatment is at cost of maintaining larger stencils. Even though the computational overhead is marginal (e.g., UC_{11} is found to be only 30% more expensive than UC_5), this imposes certain complications in coding. As a consequence, implementation of HOUC schemes on quad/octree-based AMR may be difficult.

5.1.4. The role of AMR and comparison to PLS

Practical applications of our interest here involve multiscale multiphase problems with continuous breakup of interfaces and evolving, continuously refining length scales. It is obvious that a successful modeling of these

flows requires ability to provide an adequate effective density of underlying datasets. Our approach in this regard consists of incorporating Structured Adaptive Mesh Refinement, which not only enforces the fidelity of capturing fine-grain interfacial features (at the level comparable to the best particle-based methods), but also provides an adequate resolution of near-interfacial boundary layers, when coupled with fluid dynamics solvers.

The effectiveness of SAMR is demonstrated on problems (#5–8), which involve a drastic thinning of the interface, which eventually becomes unresolvable. Illustrative results of grid refinement as afforded by AMR are shown in Figs. 12, 13, 24, 26 and 27, and Table 6.

The performance of our SAMR- and HOUC-based approach is comparable to the PLS methods by Enright et al. [8] and Hieber and Koumoutsakos [15]. Comparative analysis of mass conservation errors is presented in Table 6. The results for the interface rotation, translation and moderate stretching problems #1–4 are comparable and even better than those of the PLS method (e.g., Fig. 25). For numerical problems #7 and #8 with severe interface tearing, our $\mathrm{SAMR}^{4=4}_{8192^2}$ solutions are also comparable to the high-resolution particle-tracked ones, presented in Fig. 13b of [33] and Fig. 24 of [8]; and better than the solution by PLS-WENO_5 (Fig. 24 of [8]). Importantly, adequate resolution of thin filaments and associated physics is possible only based on *appropriately dense underlying datasets*, Eulerian (provided by SAMR) here or Lagrangian (seeded particles) in [33] and [8], both non-strictly conservative. It may be worth of noting that fully conservative interface treatments, like VOF [33], conservative LS [27], or their combinations [42], are not capable of this kind of fidelity. In fact this is a case in point where mass conservation can produce a false sense of security, as the fidelity of the interface position can really suffer (the well-known blobby structures due to numerical surface tension [19,33]). In the 3D problem #5, our AMR simulation with effective grid resolution 512^3

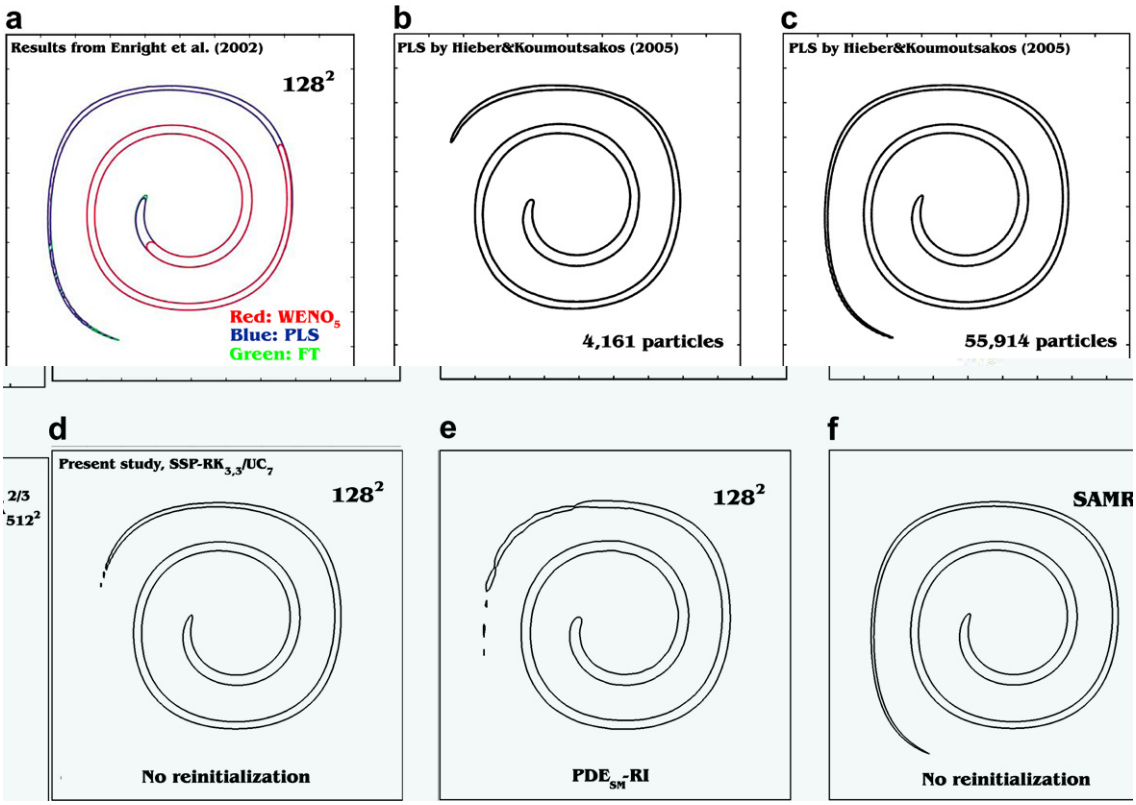

Fig. 25. Shape of interface for $t = 3$ of Problem #6. (a) WENO_5, PLS (512^2-equivalent) and highly-resolved front-tracking solutions from [8]; (b) PLS solution with remeshing and reinitialization (4161 particles, $\square 64^2$-equivalent) from [15]; (c) PLS solution with remeshing and reinitialization (55,914 particles, $\square 256^2$-equivalent) from [15]; (d–f) present study.

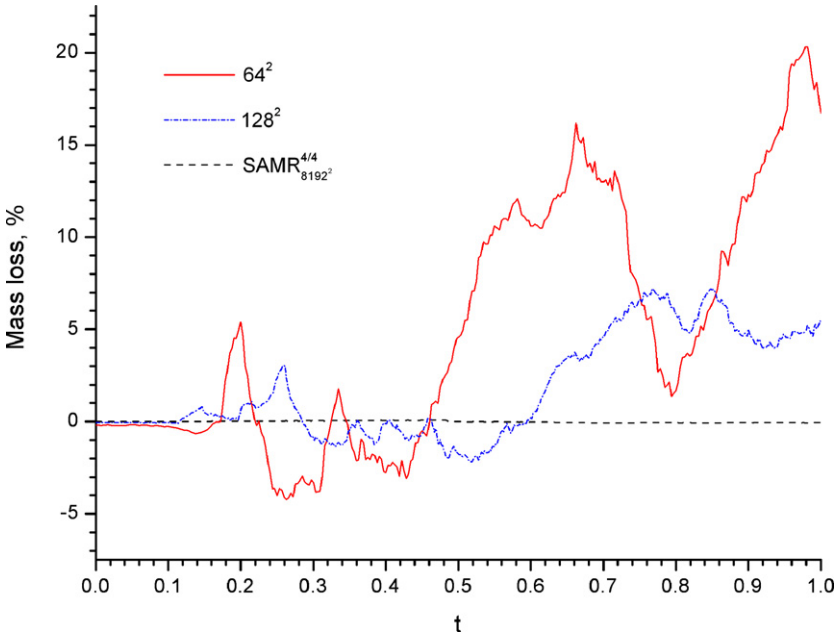

Fig. 26. History of mass conservation errors for the "2D convection/stretching in a multiple-vortex" (Problem #7). SSP-$RK_{3,3}/UC_7$ scheme.

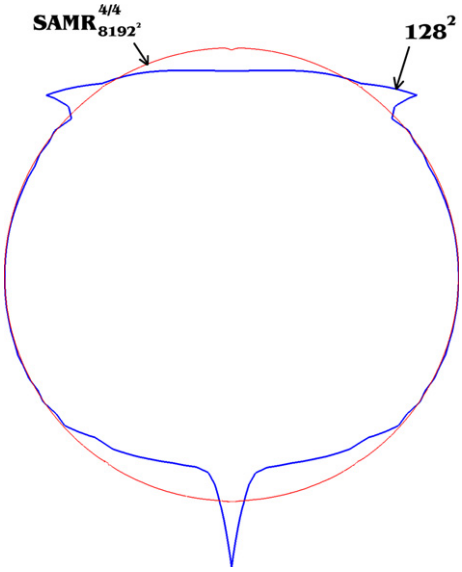

Fig. 27. Final shape of interface after one cycle of the "time-reversed 2D convection/stretching in a multiple-vortex" (Problem #8). SSP-$RK_{3,3}/UC_7$ scheme.

(Fig. 9d) is comparable to the PLS-$WENO_5$-based one [8,9], which employed initial seeding of 64 particles per interfacial cell and effectively corresponding to the same density of underlying dataset.

It is worth of noting that three-dimensional uniform 512^3 grid consists of approximately 134 million nodes, while the actual number of computational cells for $SAMR^{2=4}_{512^3}$ has varied between 9 and 20 millions. This gives an order of magnitude improvement in memory and computational speedup.

Finally, we would like to emphasize that grid adaptation by SAMR provides not only sufficiently dense underlying data structure for resolution of fine interface structures, but also *an adequate resolution of*

Table 6
Comparison to the particle level set (PLS) method

# Problem	Reference	Grid resolution	Scheme	Error
2	Enright et al. [8]	50^2	$WENO_5$	100%
			PLS-$WENO_5$	14.9%
	Present study		**$WENO_5$**[a]	**7**%
			UC_5	**3.2**%
			UC_7	**1.1**%
	Enright et al. [8]	100^2	$WENO_5$	5.3%
			PLS-$WENO_5$	0.31%
	Present study		**UC_5**	1.44%
			UC_7	**0.8**%
	Enright et al. [8]	200^2	$WENO_5$	0.54%
			PLS-$WENO_5$	0.2%
	Present study		**UC_7**	**0.16**%
4 (with $T = 8$)	Marchandise et al. [20]	64^2	DG TRI(4)	0.24%
	Enright et al. [8]	128^2	$WENO_5$	39.8%
			PLS-$WENO_5$	0.71%
	Hieber & Koumoutsakos [15]		PLS	4.2%
	Present study		**UC_7**	**2.77**%
5	Enright et al. [8]	100^3	$WENO_5$	80%
			PLS-$WENO_5$	2.6%
	Present study	50^3	**UC_7**	**15.17**%
		$SAMR^{2=2}_{128^3}$		**0.50**%
		$SAMR^{2=3}_{256^3}$		**0.45**%
		$SAMR^{2=4}_{512^3}$		**0.42**%
8	Enright et al. [8]	128^2	$WENO_5$	17.2%
			PLS-$WENO_5$	0.03%
	Present study	128^2	**UC_7**	**5.26**%
		$SAMR^{4=4}_{8192^2}$	**UC_7**	**0.039**%

[a] The difference between our's and Enright's et al. [8] $WENO_5$ results is most probably associated with different treatment of reinitialization (PDE_{SM}-based here *vs.* FM-based in [8]).

interfacial boundary layers of (compressible) fluid dynamics; while the PLS methods [8,15] are not designed for this purpose. If someone is interested in only interfacial dynamics, particle-based Lagrangian methods [8,15] are more efficient, as the total number of supported data units (particles) is smaller than the total number of SAMR cells.

5.2. "Rayleigh–Taylor instability"

A heavy fluid (density ρ_h) is placed atop of a layer of a lighter fluid (density ρ_l) in the gravitational field. Small perturbations are added to the interface, by generating the level set as

$$\varphi(\mathbf{x}) = y - H_0 - \sum_{i=0} \cos\left(\frac{2\pi\omega_i}{W}x\right); \qquad (14)$$

where W is the width of the computational domain, H_0 is the position of the undisturbed interface, $= 1.25 \times 10^{-4}$ is the amplitude of initial disturbances and ω_i are the wavenumbers involved (4, 14, 23, 28,

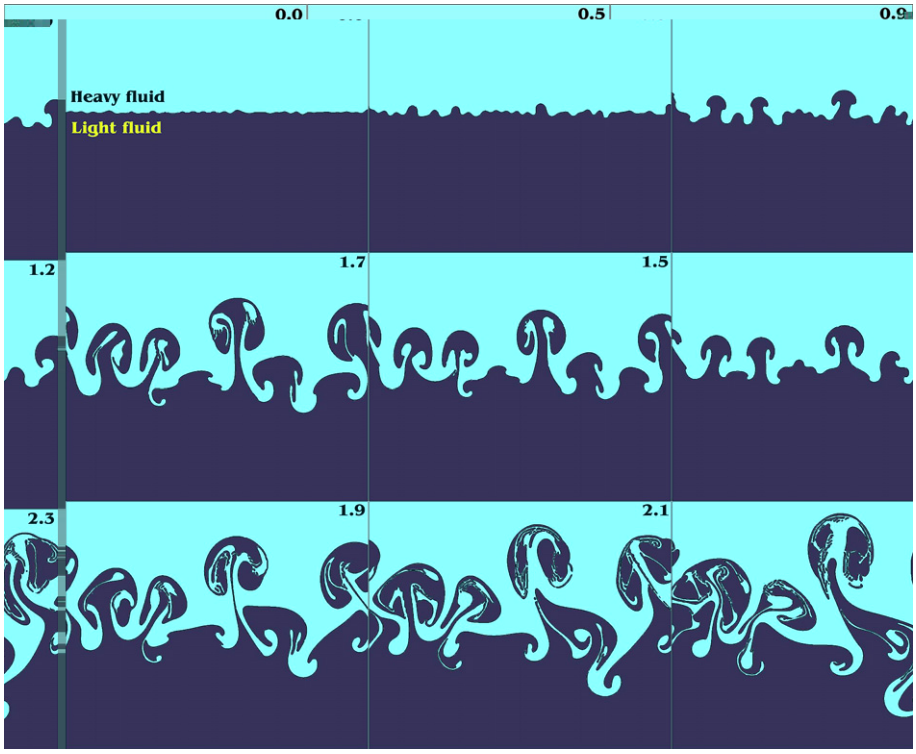

Fig. 28. Dynamics of the interface for a multi-mode Rayleigh–Taylor instability test, at $At = 0.75$, and including interfacial tension. $SAMR^{2=4}_{512=W}$.

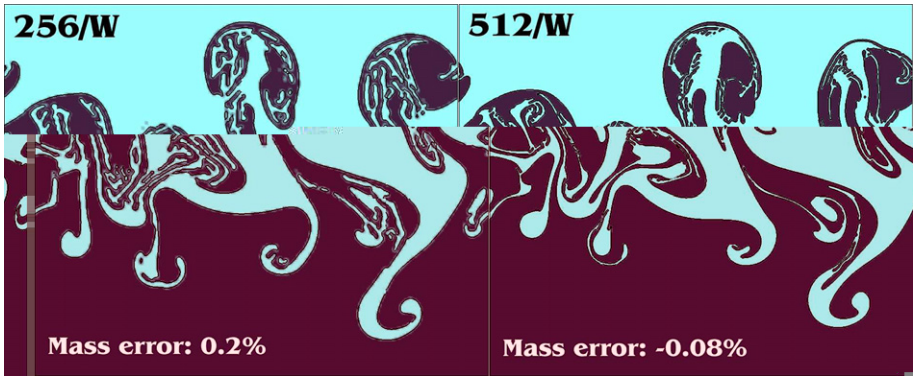

Fig. 29. Grid convergence for a multi-mode Rayleigh–Taylor instability test, $t = 2$.

Table 7
Summary of the simulation data for α_b

Youngs [45,46]	VOF	1984	α_b □ 0.04–0.05
He et al. [14]	LBE	1999	α_b □ 0.04
Glimm et al. [12]	FT	2001	α_b □ 0.07
Present study	**LS**	**2005**	α_b □ **0.06–0.07**

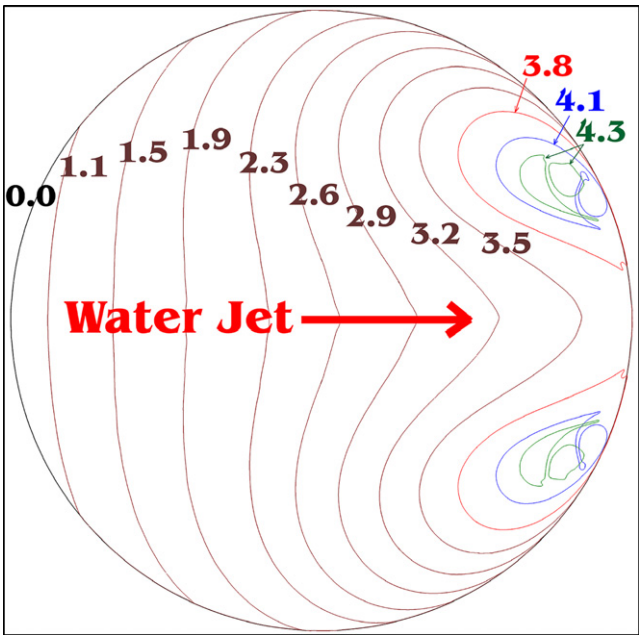

Fig. 30. Kinematics of interface during shock-induced bubble collapse. Time is shown in 1s. $SAMR^{2=6}_{800=D}$.

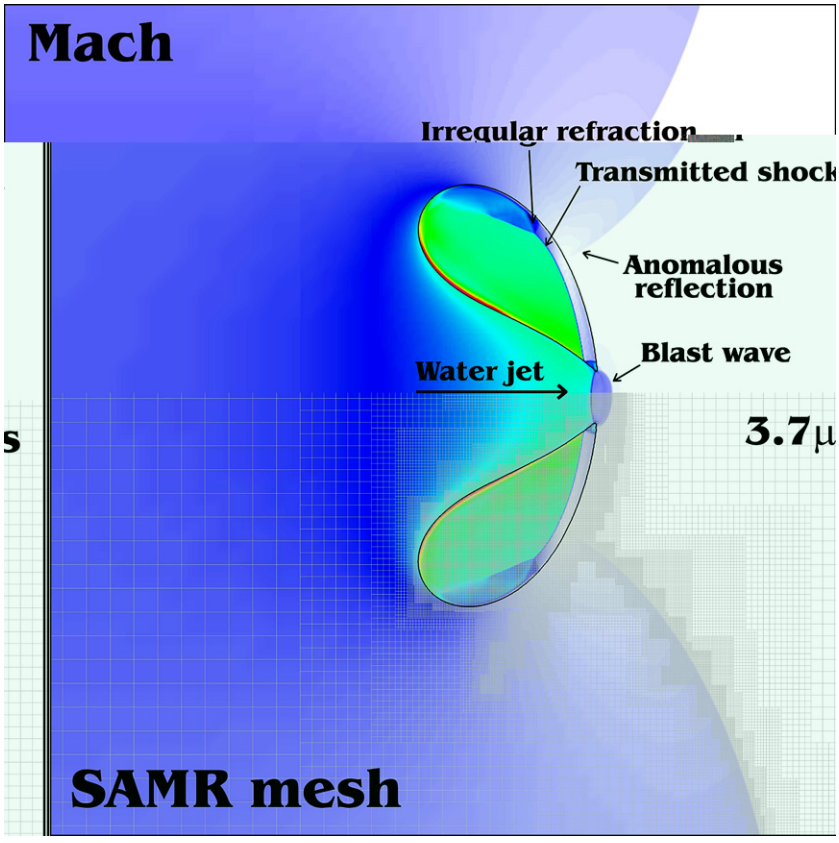

Fig. 31. Mach field and SAMR mesh for shock-induced bubble collapse. Bubble breakup stage. $SAMR^{2=6}_{800=D}$.

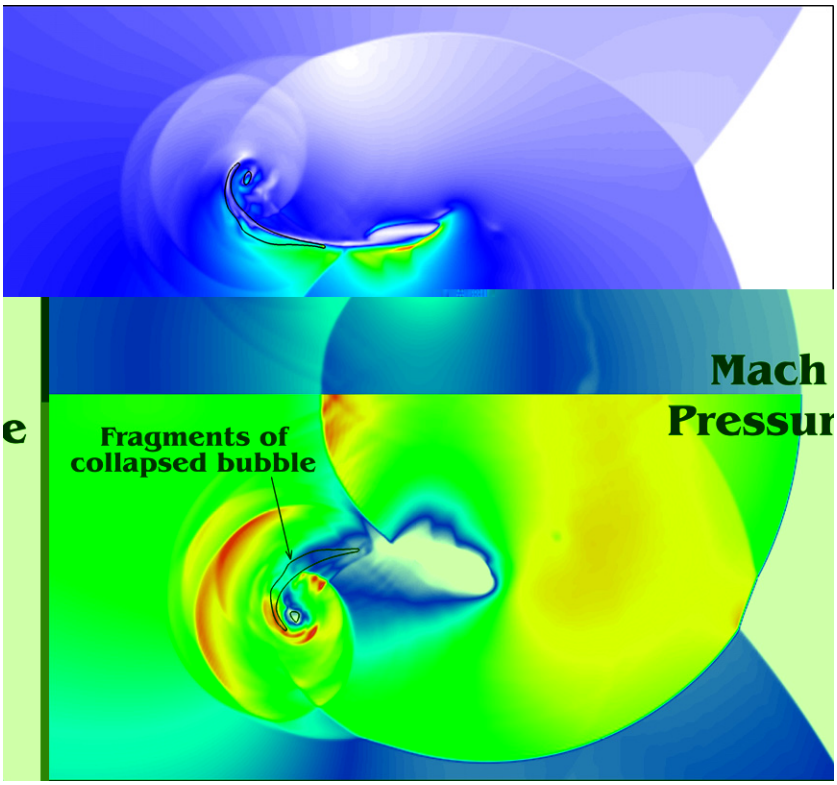

Fig. 32. Mach and pressure fields at the final stage of the shock-induced bubble collapse. $t = 4.5$ 1s. $\mathrm{SAMR}^{2=6}_{800=D}$.

33, 42, 51, 59). Simulations are started from the motionless configuration with the initial pressure field prescribed by the local hydraulic head. A density ratio $\frac{\rho_h}{\rho_l} ¼ 7$ is specified to produce an Atwood number of 0.75. The kinematic viscosities are chosen to get $Re_h = 1000$ and $Re_l = 2000$, where the Reynolds numbers are defined by $\mathrm{Re}_k ¼ \frac{\rho\sqrt{Wg}W}{\nu_k}$. Surface tension was also included and set to $\tilde{\sigma} ¼ \frac{\sigma}{\sigma_0} ¼ \frac{7}{80}$, where $\sigma_0 ¼ ð\rho_h þ \rho_l Þð g \nu_h^4 Þ^{1=3}$ (see [6]). Computations are performed in the (1×8) domain, using boundary conditions which are periodical in horizontal direction and no-slip (solid wall) at the top and bottom.

For simulation of fluid dynamics in a nearly-incompressible regime, the SSP-$\mathrm{RK}_{3,3}$/UC_7-based pseudocompressible solver for multifluid flows is applied [23,25]. Interface jump conditions (density, viscosity, stresses and surface tension) are captured sharply, as described in [25]. The level set equation is discretized using the UC_7 scheme.

Fig. 28 illustrates the dynamics of the instability progressed well into the non-linear regime with significant mixing, including severe interface deformation and stretching. There are eight distinct waves growing from the initially perturbed interface. It can be seen that at the early stage the waves grow nearly independent of each other. Eventually, strong interactions develop, causing significant turbulent-like mixing with vortex dipoles of length scales significantly larger than the initial perturbation.

The effect of grid resolution on interface structure in the non-linear regime is shown in Fig. 29. The solution is grid convergent, corresponding to the decrease of mass conservation errors from 0.2% (on the grid 256/W) to 0.08% (on the grid 512/W).

The bubble acceleration constant α_b provides the most basic characterization of the Rayleigh–Taylor instability growth in the non-linear regime, $h_b(t) = \alpha_b A t\ gt^2$, where $h_b(t) = (y_b(t) \square H_0)$ is the position of the bubble front. The ability of correct prediction of α_b was an issue for many years [12,14,45,46]. Earlier simulations tend to underpredict α_b, experimentally measured to be in the range between 0.06 and 0.07 (see [12]). Our α_b is consistent with the most recent simulations by the advanced front-tracking approach, see Table 7.

Table 8
Mass conservation errors for the "shock-induced bubble collapse"

Resolution	2.6 ls	Rate	4 ls	Rate
200/D	□3.11%	–	□20.74%	–
400/D	□1.99%	0.644	□13.87%	0.580
800/D	□1.19%	0.742	□9.64%	0.525
1600/D	□0.80%	0.573	□6.80%	0.503
3200/D	□0.52%	0.621	□4.73%	0.524

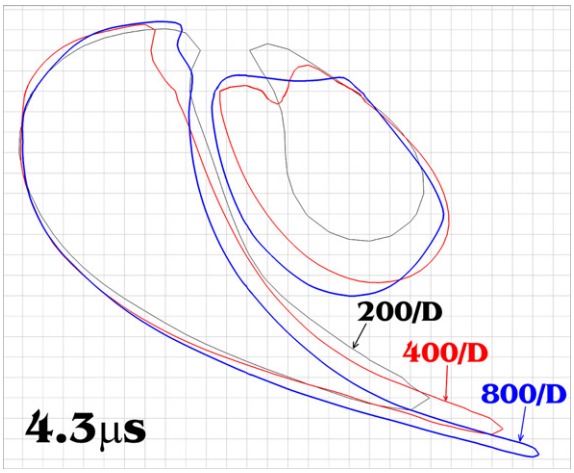

Fig. 33. Bubble resolution at the final stage of the collapse. Upper half. Black thin line: 200/D; red thicker line: 400/D; and blue thickest line: 800/D. The shown underlying mesh corresponds to resolution of 200 nodes/Dia.

5.3. "Shock-induced bubble collapse"

A 6 mm-in-diameter cylindrical air bubble is suspended in a water pool and it is hit by $M = 1.72$ shock wave coming on from the left. The center of the bubble is at $\mathbf{x}_b = (12, 12)$ mm of the computational domain (24×24) mm. Initial conditions are: $\mathbf{u} = (0, 0)$ m/s, $P = 10^5$ Pa, $\rho_{air} = 1$ kg/m^3 and $\rho_{water} = 1000$ kg/m^3 (*pre-shock*); and $\mathbf{u} = (681.58, 0)$ m/s, $P = 1.9 \times 10^9$ Pa, $\rho_{water} = 1323.65$ kg/m^3 (*post-shock*); with initial shock placed 5.4 mm to the left of the air bubble center. Parameters of the stiffened-gas EOS

$$P = (\gamma - 1)\rho i - \gamma \Pi; \quad \text{where } i \text{ is a specific internal energy}$$

are $\gamma = 4.4$, $P = 6 \times 10^8$ and $\gamma = 1.4$, $P = 0$ for water and air, respectively. BCs are periodical in the vertical direction and non-reflection at the left and right boundaries of the domain. Upon the impact by the shock, the gas bubble collapses, Figs. 30–32. For treatment of interfacial boundary conditions, the adaptive characteristics-based matching approach (aCBM) is applied [26]. Surface tension and viscosity are neglected. Here, we employed SSP-RK$_{3,3}$/WENO$_5$-based discretization of gas dynamics (see for details [26]) and UC$_7$ for the level set.

Computations were performed on a sequence of grids: $\text{SAMR}^{2=4}_{200=D}$, $\text{SAMR}^{2=5}_{400=D}$, $\text{SAMR}^{2=6}_{800=D}$, $\text{SAMR}^{2=7}_{1600=D}$ and $\text{SAMR}^{2=8}_{3200=D}$, where we use the initial diameter of bubble to indicate effective grid resolution. Mass of the gas was computed with the first-order-accurate piecewise-constant algorithm, integrating $(\rho_{(i,j)} Dx Dy)$ over all cells with negative level set.

Mass conservation errors are presented in Table 8 for time 2.6 and 4.0 ls, corresponding to mid- and final stages of bubble collapse. For the best grid of 3200 nodes/D, mass conservation is maintained below 5%, even at the latest stages of the collapse, near the grid resolution limit of the underlying dataset, see Fig. 33. With grid refinement, mass conservation errors decrease with rates varying between 0.503 and 0.742. The most severe mass losses occur for $t > 4$ ls, when thin filaments and poorly-resolved fragmented bubbles begin to develop.

6. Conclusion

We have demonstrated that high-fidelity interface tracking can be achieved within a purely Eulerian treatment of the level set method. Our approach is based on limiting numerical discretization errors as effected by combining high-order upstream central (HOUC) schemes with structured adaptive mesh refinement (SAMR). In terms of ability to describe interface structures at the limits of resolution and essentially eliminating mass conservation errors, the level of fidelity achieved is comparable to the Lagrangian-based MP and PLS methods.

The other prominent features include a new technique for anchoring the interface during PDE-reinitialization and a non-linear algorithm for interface detection during AMR tagging, allowing to eliminate spurious oscillations and improve effectiveness of adaptive mesh refinement.

The developed here Eulerian unlimited anchored adaptive level set (ua^{2}LS) is particularly useful for simulation of *compressible multifluid flows*, especially of highly unstable interfaces.

Acknowledgments

This work was carried out for the Joint Science and Technology Office, Defense Threat Reduction Agency, with the support and cooperation of Mr. C. Fromer and Dr. J. Hannan. We are also grateful to Drs. G. Nakafuji, F. Handler (LLNL), and R. Babarsky (NGIC) for continuing, long term support and collaboration. We would also like to thank Dr. Richard Hornung (LLNL) for help and kindly allowing us to use SAMRAI's utilities.

References

[1] D. Adalsteinsson, J.A. Sethian, The fast construction of extension velocities in level set methods, Journal of Computational Physics 148 (1999) 2–22.
[2] M.J. Berger, P. Colella, Local adaptive mesh refinement for shock hydrodynamics, Journal of Computational Physics 82 (1989) 67–84.
[3] M.J. Berger, J. Oliger, Adaptive mesh refinement for hyperbolic partial differential equations, Journal of Computational Physics 53 (1984) 482–512.
[4] M.J. Berger, I. Rigoutsos, An algorithm for point clustering and grid generation, IEEE Transactions on Systems, Man, and Cybernetics 21 (5) (1991) 1278–1286.
[5] D.S. Balsara, C.-W. Shu, Monotonicity preserving weighted essentially non-oscillatory schemes with increasingly high order of accuracy, Journal of Computational Physics 160 (2000) 405–452.
[6] S. Chandrasekhar, Hydrodynamic and Hydromagnetic Stability, Dover Publications Inc., New York, 1981, pp. 444–449.
[7] D.-I. Choi, J.D. Brown, B. Imbirida, J. Centrella, P. MacNeice, Interface conditions for wave propagation through mesh refinement boundaries, Journal of Computational Physics 193 (2004) 398–425.
[8] D. Enright, R. Fedkiw, J. Ferziger, I. Mitchell, A hybrid particle level set method for interface capturing, Journal of Computational Physics 183 (2002) 83–116.
[9] D. Enright, F. Losasso, R. Fedkiw, A fast and accurate semi-Lagrangian particle level set method, Computers and Structures 83 (6-7) (2005) 479–490.
[10] R.P. Fedkiw, T. Aslam, B. Merriman, S. Osher, A non-oscillatory Eulerian approach to interfaces in multimaterial flows (the ghost fluid method), Journal of Computational Physics 152 (1999) 457–492.
[11] C.A.J. Fletcher, Computational Techniques for Fluid Dynamics, second ed., vol. 1, Springer, Berlin/Heidelberg/New York, 1991.
[12] J. Glimm, J.W. Grove, X.L. Li, W. Oh, D.H. Sharp, A critical analysis of Rayleigh–Taylor growth rates, Journal of Computational Physics 169 (2001) 652–677.
[13] S. Gottlieb, On high order strong stability preserving Runge–Kutta and multi step discretizations, Journal of Scientific Computing 25 (1/2) (2005) 105–128.
[14] X. He, S. Chen, R. Zhang, A lattice Boltzmann scheme for incompressible multiphase flow and its application in simulation of Rayleigh–Taylor instability, Journal of Computational Physics 152 (1999) 642–663.
[15] S.E. Hieber, P. Koumoutsakos, A Lagrangian particle level set method, Journal of Computational Physics 210 (2005) 342–367.
[16] R.D. Hornung, S.R. Kohn, Managing application complexity in the SAMRAI object-oriented framework, Concurrency and Computation: Practice and Experience (Special Issue) 14 (2002) 347–368.
[17] G.S. Jiang, C.-W. Shu, Efficient implementation of weighted ENO schemes, Journal of Computational Physics 126 (1996) 202–228.
[18] G.S. Jiang, D. Peng, Weighted ENO schemes for Hamilton–Jacobi equations, SIAM Journal of Scientific Computing 21 (2000) 2126–2143.

[19] F. Losasso, R. Fedkiw, S. Osher, Spatially adaptive techniques for level set methods and incompressible flow, Computers and Fluids 35 (2006) 995–1010.
[20] E. Marchandise, J.-F. Remacle, N. Chevaugeon, A quadrature-free discontinuous Galerkin method for the level set equation, Journal of Computational Physics 212 (2006) 338–357.
[21] W. Mulder, S. Osher, J.A. Sethian, Computing interface motion in compressible gas dynamics, Journal of Computational Physics 100 (1992) 209–228.
[22] D. Nguyen, F. Gibou, R. Fedkiw, A fully conservative ghost fluid method and stiff detonation waves, in: 12th International Detonation Symposium, San Diego, CA, 2002.
[23] R.R. Nourgaliev, T.N. Dinh, T.G. Theofanous, A pseudo-compressibility method for the numerical simulation of incompressible multifluid flows, International Journal of Multiphase Flow 30 (7–8) (2004) 901–937.
[24] R.R. Nourgaliev, S. Wiri, T.N. Dinh, T.G. Theofanous, On improving mass conservation of level set method by reducing spatial discretization errors, International Journal of Multiphase Flow 31 (12) (2005) 1329–1336.
[25] R.R. Nourgaliev, T.N. Dinh, T.G. Theofanous, Sharp treatment of surface tension and viscous stresses in compressible multifluid dynamics, in: The 17th AIAA Computational Fluid Dynamics Conference, Toronto, Canada, June 6–9, 2005, AIAA Paper 2005-5349.
[26] R.R. Nourgaliev, T.N. Dinh, T.G. Theofanous, Adaptive characteristics-based method for compressible multifluid dynamics, Journal of Computational Physics 213 (2) (2006) 500–529.
[27] E. Olsson, G. Kreiss, A conservative level set method for two phase flow, Journal of Computational Physics 210 (2005) 225–246.
[28] S. Osher, J.A. Sethian, Fronts propagating with curvature-dependent speed: algorithms based on Hamilton–Jacobi formulations, Journal of Computational Physics 79 (1988) 12–49.
[29] S. Osher, R. Fedkiw, Level set methods and dynamic implicit surfacesApplied Mathematical Sciences, vol. 153, Springer, New York, Berlin, Heidelberg, 2003.
[30] D.P. Peng, B. Merriman, S. Osher, H. Zhao, M. Kang, A PDE-based fast local level set method, Journal of Computational Physics 155 (1999) 410–438.
[31] W.H. Press, S.A. Teukolsky, W.T. Vetterling, B.P. Flannery, Numerical Recipies in C (The Art of Scientific Computing), Second ed., Cambridge University Press, Cambridge, 1997.
[32] W.J. Rider, D.B. Kothe, Stretching and tearing interface tracking methods, in: The 12th AIAA CFD Conference, San Diego, USA, June 20, 1995, AIAA-95-1717.
[33] W.J. Rider, D.B. Kothe, Reconstructing volume tracking, Journal of Computational Physics 141 (1998) 112–152.
[34] SAMRAI: structured adaptive mesh refinement application infrastructure. Available from <http://www.llnl.gov/CASC/SAMRAI>.
[35] J.A. Sethian, Level set methods and fast marching methods, Cambridge University Press, Cambridge, 1999.
[36] C.-W. Shu, S. Osher, Efficient implementation of essentially non-oscillatory shock-capturing schemes, Journal of Computational Physics 77 (1989) 439–471.
[37] J. Strain, Tree methods for moving interfaces, Journal of Computational Physics 151 (1999) 616–686.
[38] G. Strang, Accurate partial difference methods II: non-linear problems, Numerische Mathematik 6 (1964) 37–46.
[39] M. Sussman, P. Smereka, S. Osher, A level set method for computing solutions to incompressible two-phase flow, Journal of Computational Physics 119 (1994) 146.
[40] M. Sussman, E. Fatemi, An efficient, interface-preserving level set redistancing algorithm and its application to interfacial incompressible fluid flow, SIAM Journal of Scientific Computing 20 (1999) 1165.
[41] M. Sussman, A.S. Almgren, J.B. Bell, P. Colella, L.H. Howell, M.L. Welcome, An adaptive level set approach for incompressible two-phase flows, Journal of Computational Physics 148 (1999) 81–124.
[42] M. Sussman, E.G. Puckett, A coupled level set and volume-of-fluid method for computing 3D and axisymmetric incompressible two-phase flows, Journal of Computational Physics 162 (2000) 301–337.
[43] L.B. Tran, H.S. Udaykumar, A particle-level set-based sharp interface Cartesian grid method for impact, penetration, and void collapse, Journal of Computational Physics 193 (2004) 469–510.
[44] A. Wissink, D. Hysom, R. Hornung, Enhancing scalability of parallel structured AMR calculations, in: Proceedings of the 17th ACM International Conference on Supercomputing (ICS03), San Francisco, CA, June 23–26, 2003, pp. 336–347.
[45] D.L. Youngs, Numerical simulation of turbulent mixing by Rayleigh–Taylor instability, Physica D 12 (1984) 32–44.
[46] D.L. Youngs, Three-dimensional numerical simulation of turbulent mixing by Rayleigh–Taylor instability, Physics of Fluids A 3 (1991) 1312.
[47] S. Zalesak, Fully multidimensional flux-corrected transport algorithms for fluids, Journal of Computational Physics 31 (1979) 335.